PHYSICAL REVIEW C VOLUME 51, NUMBER 3 MARCH 1995

Parity mixing of the 0^+-0^- $I=1$ doublet in ^{14}N

V. J. Zeps,* E. G. Adelberger, A. García,† C. A. Gossett,‡ and H. E. Swanson
Nuclear Physics Laboratory GL-10, University of Washington, Seattle, Washington 98195

W. Haeberli, P. A. Quin, and J. Sromicki§
Physics Department, University of Wisconsin, Madison, Wisconsin 53706

(Received 7 April 1994; revised manuscript received 16 December 1994)

We studied parity mixing of the $0_2^+, 0_1^-$; I=1 doublet in ^{14}N ($E_x \sim 8.6$ MeV) to probe the isoscalar component of the parity nonconserving (PNC) nucleon-nucleon interaction. The weak matrix element connecting the 0^+ and 0^- levels was determined by measuring the longitudinal analyzing power (A_L) over the narrow $J^\pi = 0^+$ ^{13}C($\vec{p},p$) resonance at $E_p = 1.16$ MeV. Scattered protons were detected in two arrays of four scintillators arranged symmetrically about the beam axis at mean angles of $\overline{\Theta}_1 = 35°$ and $\overline{\Theta}_2 = 155°$. The PNC signal was the difference in the longitudinal analyzing power observed at the two angles. Feedback loops were used to stabilize the position, angle, and spin direction of the beam on target. The observed signal was $A_L(\overline{\Theta}_2) - A_L(\overline{\Theta}_1) = 0.9 \pm 0.6 \times 10^{-5}$ which corresponds to a weak matrix element $\langle H_{\rm weak} \rangle = 0.38 \pm 0.28$ eV. Our measured $\langle H_{\rm weak} \rangle$ disagrees with theoretical expectations; recent shell-model calculations by Horoi *et al.* using the PNC NN amplitudes of Desplanques, Donoghue, and Holstein yield $\langle H_{\rm weak} \rangle$'s that lie in the range from -0.2 eV to -0.8 eV. We briefly discuss some theoretical uncertainties that arise because the structure of the ^{14}N doublet differs in important ways from other known parity doublets. In ancillary studies of the ^{13}C(p,γ) reaction at $\theta_\gamma = 90°$, we found that the excitation energies and widths of the 0^+ and 0^- levels were ($E_x = 8624 \pm 2$ keV, $\Gamma = 4.0 \pm 0.3$ keV) and ($E_x = 8802 \pm 7$ keV, $\Gamma = 440 \pm 8$ keV), respectively. We also determined the following partial widths: $\Gamma_\gamma(8624 \to 0) = (0.37 \pm 0.05)$ eV, $\Gamma_\gamma(8624 \to 3948) = (1.26 \pm 0.17)$ eV, $\Gamma_\gamma(8624 \to 5691) = (0.43 \pm 0.06)$ eV, $\Gamma_\gamma(8624 \to 6204) = (2.03 \pm 0.28)$ eV, and $\Gamma_\gamma(8802 \to 0) = (25.2 \pm 2.0)$ eV. We also report new parameters for the $E_x = 8062$ keV, $E_x = 9174$ keV, and $E_x = 9388$ keV levels.

PACS number(s): 24.80.Dc, 27.20.+n, 21.30.+y, 24.70.+s

I. INTRODUCTION

The parity-nonconserving (PNC) nucleon-nucleon (N-N) interaction is the only accessible example of a flavor-conserving hadronic weak process. At low energies ($E_{\rm c.m.} \le 50$ MeV) the PNC N-N interaction may be characterized phenomenologically in terms of the amplitudes of the five allowed $s \leftrightarrow p$ transitions [1]. In this energy regime it is appropriate to analyze the PNC interaction using parity-violating meson-exchange theory, where the weak interaction physics is confined to a meson-nucleon-nucleon (MNN) vertex [2]. In practice, seven different MNN coupling constants involving $\pi^\pm$, ρ, and ω mesons are employed, but experiments can determine only six linear combinations of these seven constants [1].

Despite considerable effort leading to a wealth of PNC measurements in complex nuclei and in the N-N system itself (for a detailed review see Ref. [1]) only a handful of experiments have provided useful information on these coupling constants. In the N-N system, for example, definite effects have been observed only in $p+p$ scattering [3–6]; measurements of PNC observables in the $n+p$ system [7,8] are not yet sensitive enough to provide useful constraints. Because of the small size of expected PNC effects in the N-N system and the small number of practical observables, one must to turn to parity violation in complex nuclei to constrain the weak N-N interaction. Complex nuclei offer a much larger number of possible PNC experiments, and occasionally one finds "accidents" of nuclear structure that greatly amplify the PNC observables and isolate certain isospin components of the interaction. On the other hand, the interpretation of these measurements in terms of the fundamental PNC N-N interaction can be obscured by uncertainties in the nuclear structure calculations needed to extract the N-N parameters from the many-body observable.

The most readily interpretable PNC measurements in complex nuclei involve isolated opposite-parity doublets in light nuclei where nearly all the parity-mixing strength resides in a single weak matrix element. Thus a single well-defined quantity can be extracted from a given measurement. Furthermore, one expects the shell model to reproduce accurately the important components of the many-body wave functions, and thus to give a reliable means of extracting the PNC N-N information from the

---

*Present address: Department of Physics and Astronomy, University of Kentucky, Lexington, KY 40506.

†Present address: Physics Department, University of Notre Dame, Notre Dame, IN 46556.

‡Present address: The Boeing Company, Seattle, WA 98124.

§Present address: Institut für Teilchenphysik, ETH-Zürich, CH-8093 Zurich, Switzerland.

PNC effect.

To date, parity-mixed doublets have been studied in ^{18}F [9–12], ^{19}F [13,14], and ^{21}Ne [15]. Together with longitudinal analyzing power (A_L) measurements in $\vec{p}+p$ and $\vec{p}+\alpha$ scattering [16], these doublets provide the most useful data for elucidating the PNC N-N interaction parameters. This data set has been analyzed by Adelberger and Haxton [1] in terms of the two dominant weak coupling constants F_π (isovector weak $\pi^\pm$ exchange) and F_0 (isoscalar weak ρ exchange). Results of this two-parameter analysis are shown in Fig. 1. The bands indicate $\pm 1\sigma$ error bars of each measurement. The "best value" from the bag model prediction of Desplanques, Donoghue, and Holstein (DDH) [2] is shown, with the double bars along the edges of the plot indicating the "reasonable ranges" of the predictions. Most of the nuclear structure uncertainties have been removed from the interpretation of the ^{18}F and ^{19}F results by calibrating the predicted many-body nuclear matrix elements in terms of the observed rates of first-forbidden β decays in ^{18}Ne and ^{19}Ne that are isospin analogs of the PNC mixing [17–19]. Thus, the ^{18}F and ^{19}F constraints on F_π and F_0 are on relatively firm ground. The ^{21}Ne constraint is dashed because it is not possible to calibrate the nuclear matrix element in this way as neither member of the ^{21}Ne doublet is the isospin analog of a ground state; hence a relatively large uncertainty is attached to the shell-model calculation. The $\vec{p}+p$ results are not displayed in Fig. 1 because, in contrast to the cases which are included, the PNC effect in $\vec{p}+p$ system is expected to have a strong isotensor contribution.

While the data set is sparse, the two-parameter analysis reveals several of the important issues:

(1) The ^{18}F result, which determines F_π, is much smaller than the DDH "best value" prediction.

(2) Because F_π is very small, the ^{19}F and $\vec{p}+\alpha$ measurements suggest that F_0 is larger than anticipated.

(3) If the ^{21}Ne shell-model calculation is correct, there are serious discrepancies in the meson-exchange picture of the PNC N-N interaction. However, before any firm conclusion can be drawn, other measurements that can be more reliably interpreted are required.

(4) Finally, none of these measurements is sensitive only to F_0. Although a remarkably precise value has been reported for an observable sensitive only to F_0, $\Gamma_{\rm PNC}[^{16}{\rm O}(2^-;0)\rightarrow{}^{12}{\rm C}_{\rm g.s.}+\alpha]=1.03\pm0.28\times10^{-10}$ eV [20], it is difficult to extract a quantitative constraint from this datum. Admixtures of several 2^+ states contribute to this decay so it cannot be analyzed using two-level mixing theory. The interpretation is further complicated because one of these admixed 2^+ states lies below the α-decay threshold so that its α width cannot be directly measured.

Much effort has been expended on studying the PNC effects in the systems discussed above, and without major improvements in experimental techniques, significantly better experimental information on the weak N-N interaction cannot be expected from these systems. Additional constraints will probably require studies of new systems that probe different combinations of MNN couplings [21]. In this paper we describe such an experiment, with primary attention paid to the experimental result. The interpretation of the unexpected result is discussed briefly; a more complete analysis will be published later. Further details may be found in Ref. [22].

A. Parity mixing in ^{14}N

Adelberger *et al.* [23] noted that the isolated $0^+,0^-;I=1$ doublet in ^{14}N at $E_x\approx8.6$ MeV is a promising system for probing the isoscalar component of the PNC N-N interaction, and that results from this doublet would complement those from existing PNC measurements. The important features of this doublet are shown in Fig. 2.

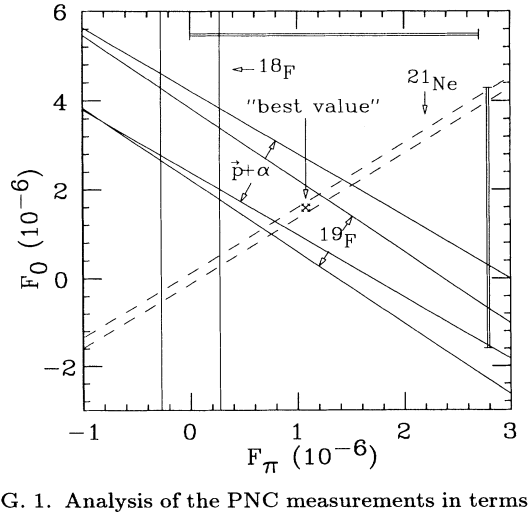

FIG. 1. Analysis of the PNC measurements in terms of the two dominant PNC MNN coupling constants F_π and F_0.

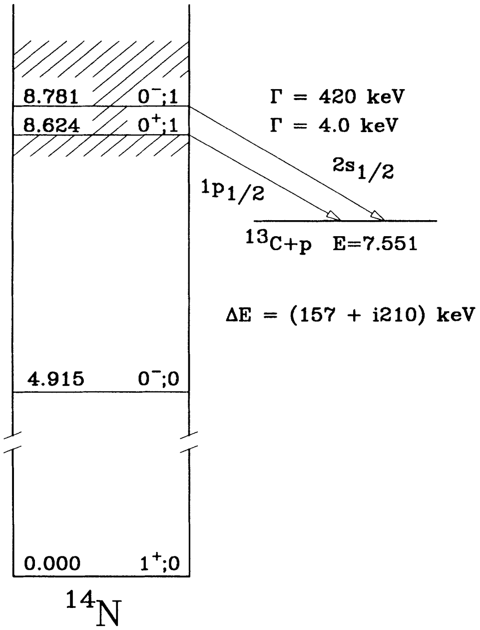

FIG. 2. The 8.6 MeV $J=0$ parity doublet of ^{14}N.

(1) The levels are closely spaced ($\Delta E = 157$ keV). The parity mixing is therefore enhanced by the small energy denominator in the perturbation expansion of the PNC mixing amplitude.

(2) The levels have very different widths ($\Gamma_{0^+} = 4.0 \pm 0.3$ keV, $\Gamma_{0^-} \approx 420$ keV) for decay to ${}^{13}\text{C}_{\text{g.s.}} + p$. Therefore, a small admixture of the short-lived 0^- level into the long-lived 0^+ level will amplify PNC observables involving proton decay of the 0^+ level. The 0^+ level decays by emitting a $p_{1/2}$ proton, while the 0^- level emits an $s_{1/2}$ proton. If the levels are parity mixed, interference between these two partial waves causes the decay protons to be longitudinally polarized. This *proton* longitudinal polarization is analogous to the γ-ray circular polarization resulting from $E1/M1$ mixing of the opposite parity $J = 0$ levels in ^{18}F.

(3) The system is isolated. The next nearest known [24] $J = 0$ state, the $0_1^-;0$ level at $E_x = 4.95$ MeV, lies more than 3 MeV away and has an energy denominator 23 times greater than the splitting of the parity doublet. (Based on the known [24] spectrum of ^{14}C, the $0_3^+;1$ level is expected to have an excitation of $E_x \approx 11.8$ MeV and a very narrow decay width—the analog level in ^{14}C has a width of 18 keV [24].) Furthermore, the $0_1^-;1$ level exhausts nearly the full single-particle width estimate; there can be no other 0^- levels with substantially greater proton decay strength. In fact, no other $0^-;1$ levels are known in the A=14 nuclei. Consequently, it is unlikely that any other 0^- level can compete favorably in producing the PNC $2s_{1/2}$ decay amplitude of the $0_2^+;1$ level. Thus the two-level mixing approximation for the circular polarization of the decay protons from the $0_2^+;1$ level is valid, which considerably simplifies the shell-model interpretation of the parity impurity.

(4) The levels are believed to have fairly simple nuclear structure. The $0_1^+;1$ level is expected to have a nearly pure $1p^{-2}$ ($0\hbar\omega$) configuration, leaving the $0_2^+;1$ level with a fairly pure $2\hbar\omega$ configuration. The spectroscopic factors [25] of the two 0^+ states [$S(0_1^+) = 1.8$ and $S(0_2^+) = 0.04$], and the large energy splitting between the levels support this contention. The $0^-;1$ level has the particularly simple single-particle structure of a $2s_{\frac{1}{2}}$ nucleon coupled to the A=13 ground state; the spectroscopic factor [26] ($S = 1.02$) supports this contention as well. Because both states of the doublet are expected to have fairly pure configurations, shell-model calculations relating the weak matrix element to the PNC N-N interaction should be relatively straightforward.

(5) Both members of the doublet are $I = 1$ states in a self-conjugate nucleus. Therefore $\Delta I = 1$ mixing is forbidden while both $\Delta I = 0$ and $\Delta I = 2$ parity mixing are allowed. As $\Delta I = 2$ matrix elements cannot have a contribution from a self-conjugate core [1], $\Delta I = 2$ mixing is expected to be negligible (down by a factor of $\approx 1/A$ compared to the $\Delta I = 0$ strength). Thus, the parity mixing is essentially isoscalar and sensitive only to the F_0 parameter of Fig. 1.

(6) Finally, in contrast to previous parity-doublet experiments that measured the $E1/M1$ mixing ratios of decay γ rays, the interpretation of the PNC observable in ^{14}N requires knowing the strong-interaction matrix elements for emitting longitudinally polarized protons. Hadronic decays are usually difficult to describe accurately because of multichannel coupling effects. The ^{14}N system is particularly simple in this regard as the two levels of interest have no channel coupling (except through parity violation). For conserved parity, the 0^+ state decays uniquely into the $l = s = 1$ channel, while the 0^- state decays into the $l = s = 0$ channel. Furthermore, the elastic channel is the only open particle decay channel, so that the phase shifts are real and readily extractable from an analysis of ${}^{13}\text{C}(p,p)$. The strong interaction problem is thus greatly simplified, and the ^{14}N PNC observable is almost as simple to interpret as the circular polarization of the 1081 keV γ ray in ^{18}F.

When this experiment began, two shell-model predictions for the PNC nuclear matrix element, based on the "best value" PNC N-N interaction of Desplanques, Donoghue, and Holstein [2], were available. Adelberger *et al.* [23] reported a calculation using the Zuker-Buck-McGrory basis which gave a parity-violating matrix element of -1.39 eV. Dubach and Haxton [27] made a complete $2\hbar\omega$ calculation and obtained a matrix element of -1.04 eV. The significance of the signs of these matrix elements is discussed below.

B. Parity mixing of elastic scattering resonances

We measured the circular polarization of the decay protons by reversing the reaction and polarizing the protons of the incoming channel. The PNC observable was the helicity dependence of the ${}^{13}\text{C}(\vec{p},p)$ cross section over the 0^+ and 0^- resonances. Specifically, we measured the longitudinal analyzing power (A_L):

$$A_L \equiv \frac{1}{|P_z|}\,\frac{\sigma^+ - \sigma^-}{\sigma^+ + \sigma^-}\,, \tag{1.1}$$

where $\sigma^+(\sigma^-)$ is the cross section for positive (negative) helicity protons, and P_z is the beam's longitudinal polarization. Our measurement was the first attempt to observe parity mixing of elastic scattering resonances.

The reaction theory for parity-mixed elastic scattering resonances can be described [23] using Bloch's S-matrix formalism [28]. Assuming that the parity violation results only from parity mixing of the two levels, that no other levels of like J^π need to be considered simultaneously (single-level approximation), and that each resonance had a a unique channel spin, Adelberger *et al.* showed that the parity violating part of the S matrix is

$$S^J_{l_1S_1,l_2S_2} = -ie^{i(\xi_{l_1}+\xi_{l_2})}\,\frac{\mathbf{G}^J_{l_1S_1}\mathbf{G}^J_{l_2S_2}\langle l_1S_1,J|H_{\text{PNC}}|l_2S_2,J\rangle}{\left(E - E^{J,\pi_1} + \frac{i}{2}\Gamma^J_{l_1S_1}\right)\left(E - E^{J,\pi_2} + \frac{i}{2}\Gamma^J_{l_2S_2}\right)}\,, \tag{1.2}$$

where the **G**'s are width amplitudes which may have either sign, and the matrix element element $\langle l_1 S_1, J | H_{\mathrm{PNC}} | l_2 S_2, J\rangle$ is a real quantity. The level width Γ^J_{lS} is related to $\mathbf{G}^J_{lS}$ by $\Gamma^J_{lS} = (\mathbf{G}^J_{lS})^2$.

The parity conserving part of the S matrix has the usual form

$$S^J_{l_1S_1,l_2S_2} = e^{i(\xi_{l_1}+\xi_{l_2})}\left[\delta_{S_1S_2}\delta_{l_1l_2} - i\frac{\mathbf{G}^J_{l_1S_1}\mathbf{G}^J_{l_2S_2}}{\left(E - E^{J,\pi} + \frac{i}{2}\Gamma^J\right)}\right], \tag{1.3}$$

where l and S are the channel orbital and spin quantum numbers, J and π are the resonance total angular momentum and parity, $E^{J,\pi}$ is the resonance energy, and Γ^J_{lS} is the partial width of the level. The nonresonant phase shifts ξ_l are the sum of Coulomb and hard-sphere phase shifts:

$$e^{2i\xi_l} = \frac{G_l(k_pa_\lambda) - iF_l(k_pa_\lambda)}{G_l(k_pa_\lambda) + iF_l(k_pa_\lambda)}\exp^{2i(\sigma_l-\sigma_0)}, \tag{1.4}$$

where the Coulomb phase shift is given by

$$\sigma_l - \sigma_0 = \sum_{s=1}^{l}\tan^{-1}\eta/s, \tag{1.5}$$

with $\eta = Z_1Z_2e^2/\hbar v$. The cross section for a polarized proton beam and polarization insensitive detectors has the general form

$$\frac{d\sigma}{d\Omega} = K_U(\theta,E) + K_L(\theta,E)\vec{\sigma}\cdot\hat{k}_{\mathrm{in}} + K_T(\theta,E)\vec{\sigma}\cdot\hat{n} + K_T^*(\theta,E)\vec{\sigma}\cdot\hat{b}, \tag{1.6}$$

where $\vec{n} = \vec{k}_{\mathrm{in}}\times\vec{k}_{\mathrm{out}}$ and $\vec{b} = \vec{n}\times\vec{k}_{\mathrm{in}}$. The partial cross sections K can be calculated using Eqs. (1.2) and (1.3). The analyzing powers are obtained from the spin-dependent cross sections K_L, K_T, and K_T^* and the spin-independent cross section K_U:

$A_T = K_T/K_U$ (transverse),
$A_L = K_L/K_U$ (PNC longitudinal),
$A_T^* = K_T^*/K_U$ (PNC transverse).

The PNC transverse analyzing power A_T^*, discussed by Bizzeti [29], is not suited to probe parity mixing in ^{14}N as the interference of $J = 0$ resonances cannot contribute to A_T^* [23]. We therefore neglect A_T^* in the analysis described below.

For the idealized case of an isolated parity-mixed $J = 0$ doublet, as in ^{13}C+p,

$$K_U^{J=0}(\theta,E) = \frac{1}{k^2}|C(\theta)|^2 + \frac{1}{4k^2}\mathrm{Re}\left[iC(\theta)(T^*_{0,0} + \cos\theta T^*_{1,1})\right] + \frac{1}{16k^2}(|T_{0,0}|^2 + |T_{1,1}|^2), \tag{1.7}$$

$$K_T^{J=0}(\theta,E) = -\frac{1}{8k^2}\sin(\theta)\mathrm{Re}[C(\theta)T^*_{1,1}], \tag{1.8}$$

$$K_L^{J=0}(\theta,E) = -\frac{1}{4k^2}(1+\cos\theta)\mathrm{Re}[iC(\theta)T^*_{0,1}] - \frac{1}{8k^2}\mathrm{Re}[T_{0,1}(T^*_{0,0} + T^*_{1,1})], \tag{1.9}$$

where $C(\theta) = (\eta/2)\csc^2(\theta/2)\exp[-2i\eta\ln(\sin\theta/2)]$, and the T matrix is related to the S matrix by

$$T^J_{l_1s_1,l_2s_2} = e^{2i(\sigma_{l_1}-\sigma_0)}\delta_{l_1l_2}\delta_{s_1s_2} - S^J_{l_1s_1,l_2s_2}. \tag{1.10}$$

As the J=0 resonances have either $l = S = 0$ or $l = S = 1$, the l, S indices are combined in Eqs. (1.7)–(1.9); e.g., $T_{l_1=S_1=0,l_2=S_2=0} \equiv T_{0,0}$.

C. The phase of the PNC matrix element and the sign of A_L

The relation between the ^{13}C$(\vec{p},p)$ PNC analyzing power and the $s \leftrightarrow p$ PNC matrix element is given in Eq. (1.2). In this subsection we discuss the relation between this matrix element, the shell-model PNC matrix element connecting the 0_2^+ and 0_1^- levels of ^{14}N, and the longitudinal analyzing power A_L.

The phase of the shell-model PNC matrix element depends on the diagonalization scheme which produced the 0^+ and 0^- wave functions. However, this arbitrary phase has no physical consequences because the experimental observable is proportional to the product of $2s_{1/2}$ and $1p_{1/2}$ decay amplitudes times the weak matrix element, and all arbitrary phases enter twice. Thus, a calculation of the observable requires not only the weak matrix element, but also the signs of the strong decay amplitudes.

In the S-matrix approach the relevant phases reside in the numerator of Eq. (1.2). We express the numerator as

$$\mathbf{G}_{0^-}\mathbf{G}_{0^+}\langle 0^-|H_{\mathrm{PNC}}|0^+\rangle \equiv \sqrt{\Gamma_{0^-}\Gamma_{0^+}}\langle H_{\mathrm{weak}}\rangle, \tag{1.11}$$

where the Γ's are positive real quantities which can be taken from experiment, and the quantity $\langle H_{\mathrm{weak}}\rangle$ has a definite phase which determines the sign of the experimental effect in A_L. Following arguments detailed in Ref. [1], one can show that $\langle H_{\mathrm{weak}}\rangle$ is related to shell-model quantities by

$$\langle H_{\mathrm{weak}}\rangle \equiv -i\,\mathrm{sgn}\left[\frac{\langle {}^{13}\mathrm{C}_{\mathrm{g.s.}}|||\tilde{a}_{2s_{1/2}}|||0^-\rangle}{\langle 0^+|||a^\dagger_{1p_{1/2}}|||{}^{13}\mathrm{C}_{\mathrm{g.s.}}\rangle}\right] \times\langle 0^-||H_{\mathrm{PNC}}||0^+\rangle\ . \tag{1.12}$$

This quantity, which is independent of any arbitrary phases of the shell-model matrix elements, is real because the shell-model PNC matrix element is imaginary. By inserting (1.11) into (1.2), we obtain predictions for A_L that, except for $\langle H_{\mathrm{weak}}\rangle$ itself, involve only readily measurable quantities such as level widths and energies.

II. PROPERTIES OF THE 0^+, 0^- DOUBLET

The parity-conserving properties of the $0_2^+;1$ and $0_1^-;1$ levels of ^{14}N, as known prior to the measurements de-

TABLE I. Properties of low-lying ^{13}C(p,γ) and ^{13}C(p,p) resonances [30].

$E_p^{\rm lab}$ (keV)[a]	$\Gamma_{\rm c.m.}$ (keV)[a]	l_p	$\omega\Gamma_\gamma$ (eV)[a]	$J^\pi;T$	^{14}N* (MeV)[a]
551 ± 1	30 ± 1	0	6.5 ± 0.5 [9.2]	$1^-;1$	8.062
1156 ± 2 [1150 ± 2]	4.0 ± 0.3 [7 ± 1]	1	1.03 ± 0.07 [1.3]	$0^+;1$	8.624 [8.618]
1347 ± 7 [1340 ± 50]	440 ± 8 [~ 460]	0	6.3 ± 0.5 [12.8]	$0^-;1$	8.802 [8.79]
1462 ± 3	16 ± 2	2	0.72	$3^-;1$	8.907
1523 ± 2	8 ± 2	1,(3)	0.13	$2^+;0$	8.980
1700.5 ± 1	< 1			$3^+;0$	9.1287
1747.6 ± 0.9	135 ± 8	1	$\Gamma_{\gamma_0} = 7.2 \pm 0.4$	$2^+;1$	9.1724
			$\Gamma_p\Gamma_{\gamma_0}/\Gamma = 7.3 \pm 0.5$	(this work)	
1980 ± 3	13 ± 3	2		3^- [$3^-,2^-$]	9.388
2110 ± 3	41 ± 2	2	7.0 ± 1.0	$2^-;1$	9.509
2319 ± 4	15 ± 3	1	0.11 ± 0.01	1^+	9.703
2743	12 ± 3	1	0.37 ± 0.03	$1^+(2^+)$	10.1
3105 ± 5	33 ± 3	1	22.8 ± 1.3	$2^+;1$	10.432
6200 ± 100	1000 ± 150	2	≥ 200[b]	$2^-;1$[c]	13.3

[a] Quantities in square brackets have been superceded by this work.

[b] $(2J+1)\Gamma_{\gamma_0}$

[c] We adopt the most likely $2^-;1$ assignment for the fitting procedure.

scribed below, are shown in Tables I and II. The uncertainties in the widths and energies of these levels were large enough to produce a > 30% uncertainty in the weak matrix element corresponding to a given longitudinal analyzing power. We therefore remeasured the level parameters using the ^{13}C(p,γ) reaction at 90°. This reaction was chosen over ^{13}C(p,p) to avoid the strong Coulomb contribution to the scattering cross section. By detecting the γ rays at 90° the narrow p-wave resonances did not interfere with the dominant s-wave structure. The ^{13}C(p,γ) cross sections were analyzed with the same Breit-Wigner formulation that was employed in the elastic scattering theory used to interpret our longitudinal analyzing power results.

The ^{13}C(p,γ) cross section was studied by bombarding an $\sim$80 μg/cm^2 carbon target enriched to $\sim$ 95% in ^{13}C with an unpolarized proton beam from the University of Washington FN tandem accelerator. The incident proton energy was varied from 0.45 MeV to 3.0 MeV in steps of 0.3 keV to 50 keV, depending on the sharpness of the resonance structure. The 90° ^{13}C(p,γ) yields were measured simultaneously in an actively shielded 25.4 cm×25.4 cm NaI detector and a large-volume Ge(Li) detector. The NaI detector had a high and well-calibrated absolute γ-ray efficiency (the uncertainty in the calibration was around ±3% in the energy range of interest [31]), while the Ge(Li) detector provided higher resolution to isolate specific transitions. It was noteworthy that we were able to take data down to energies below the $1^-;1$ resonance at $E_p^{\rm lab} = 0.551$ MeV. A three-point beam energy calibration was made using the narrow resonances [32] in ^{27}Al(p,γ) at $E_p^{\rm lab} = 991.9$ keV and 1381.6 keV, and the narrow ^{13}C(p,γ) resonance [24] at $E_p^{\rm lab} = 1747.6$ keV. A total uncertainty of $\Delta E_p = \pm 2$ keV was assigned to the energy calibration.

We determined the target thickness and beam energy resolution by measuring the γ_0 yield over the narrow ($\Gamma \sim$ 135 eV [24]) ^{13}C(p,γ) resonance at $E_p^{\rm lab} = 1.75$ MeV (see

TABLE II. γ-ray decays of the $1_1^-;1$, $0_2^+;1$, and $0_1^-;1$ levels in ^{14}N.

Initial state		Final state			Branching	Strength
$J^\pi;T$	E_i (MeV)	$J^\pi;T$	E_f (MeV)	Multipole	ratio(%)[a]	(W.u.)[a,b]
$1_1^-;1$	8.06	$1_1^+;0$	0.0	$E1$	79.1 ± 0.4 [80.3 ± 0.6]	0.033 ± 0.002 [0.048]
		$0_1^+;1$	2.31	$E1$	1.2 ± 0.7 [1.4 ± 0.14]	0.0014 ± 0.0008 [0.0023]
		$1_2^+;0$	3.95	$E1$	12.6 ± 0.6 [12.7 ± 0.4]	0.039 ± 0.004 [0.057]
		$0_1^-;0$	4.92	$M1$	1.7 ± 0.4 [1.86 ± 0.14]	0.24 ± 0.06 [0.35]
		$2_1^-;0$	5.11	$M1$	0.8 ± 0.4 [0.25 ± 0.14]	0.13 ± 0.06 [0.056]
		$1_1^-;0$	5.69	$M1$	4.5 ± 0.4 [3.5 ± 0.4]	1.40 ± 0.16 [1.5]
$0_2^+;1$	8.62	$1_1^+;0$	0.0	$M1$	0.09 ± 0.01 [0.23]	0.028 ± 0.004 [0.089]
		$1_2^+;0$	3.95	$M1$	0.30 ± 0.02 [0.24]	0.60 ± 0.08 [0.59]
		$1_1^-;0$	5.69	$E1$	0.12 ± 0.01 [0.13]	0.044 ± 0.006 [0.069]
		$1_3^+;0$	6.20	$M1$	0.49 ± 0.02 [0.40]	7.0 ± 0.9 [7.1]
$0_1^-;1$	8.80	$1_1^+;0$	0.0	$E1$	≥ 0.97 [> 0.90]	0.093 ± 0.008 [0.17 ± 0.05]

[a] Quantities in square brackets are the accepted values of Ref. [24].

[b] Weiskopf units were calculated using the same prescription employed in Ref. [24].

Fig. 3). Results were analyzed with a program (THICK-TARGET) that calculated γ yields by Monte Carlo simulations of the discrete energy losses of the protons as they traverse the target [31,33]. For this narrow level, the observed shape of the resonance was almost entirely determined by the energy loss function of the target and the beam energy resolution (which was assumed to have a Gaussian form). We obtained values for the target thickness and beam energy spread of 80.2 ± 3.0 μg/cm^2 and 600 ± 150 eV, respectively.

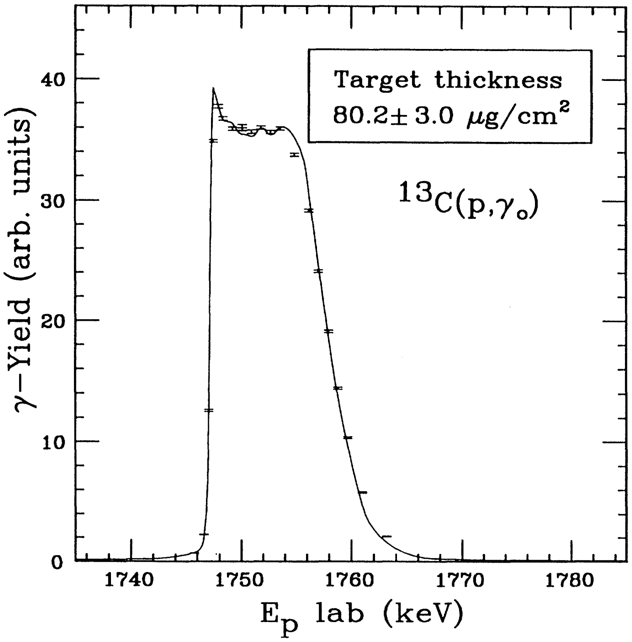

FIG. 3. ^{13}C(p,γ) excitation function across the 135 eV wide resonance at $E_p = 1.75$ MeV. The apparent width of the resonance is due to the energy loss through the target and corresponds to a target thickness of 80.2 ± 3.0 μg/cm^2.

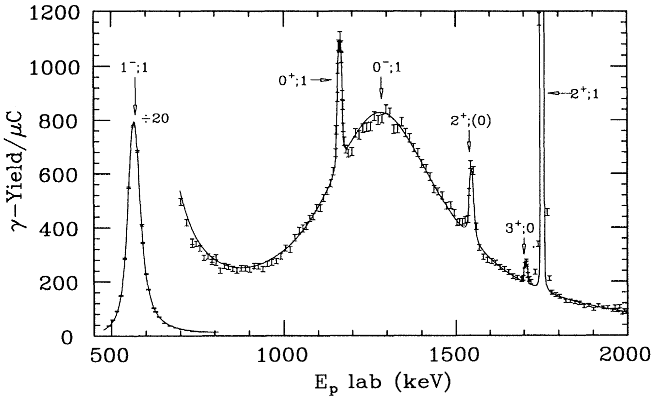

FIG. 4. Excitation function of the ^{13}C(p,γ_0) reaction. The solid curve is a fit based on the S-matrix formalism outlined in the text.

Figure 4 shows a ^{13}C(p,γ_0) excitation function taken with the above target. The $0_2^+;1$, $0_1^-;1$, and $1_1^-;1$ levels were prominent; other resonances, labeled according to their spin-parity assignments, were also observed. After correcting for the Ge(Li) efficiency, the ^{13}C(p,γ_0) yield was fitted as a sum of noninterfering Breit-Wigner resonances (using the levels listed in Table I), plus a nonresonant $E1$ direct capture (DC) term and its interference with the resonances [34]. These yields were then averaged over the target thickness with additional smearing to account for the beam energy spread and straggling effects.

The contribution of the ith resonance to the (p,γ) cross section in the center-of-mass frame was assumed to be

$$\sigma_r^i(E_p) = \frac{\pi}{k_p^2}\frac{(2J_i+1)}{(2J_p+1)(2J_t+1)}\frac{\Gamma_{\gamma_i}(E_p)\Gamma_{p_i}(E_p)}{(E_p-E_i)^2+\frac{1}{4}\Gamma_i(E_p)^2}, \tag{2.1}$$

where k_p and E_p are the incident proton wave number and center-of-mass energy. E_i is the energy and $\Gamma_{\gamma_i}(E_p)$ and $\Gamma_{p_i}(E_p)$ are the energy dependent γ and proton partial widths for the ith resonance. $\Gamma(E_p) = \Gamma_\gamma(E_p) + \Gamma_p(E_p)$, and J_p, J_t, and J_i are the projectile, target, and resonance total angular momenta, respectively. The proton width at resonance, Γ_p, was corrected for the Coulomb penetrability $P_l(E_p)$ using the standard prescription

$$\Gamma_p(E_p) \approx \Gamma_p \frac{P_l(E_p)}{P_l(E_i)}, \tag{2.2}$$

while the γ-decay width at resonance, Γ_γ, was modified by the phase space available for the electromagnetic multipole transition; for pure $E\ell$ or $M\ell$ multipoles,

$$\Gamma_\gamma(E_p) = \Gamma_\gamma \left[\frac{Q+E_p}{Q+E_i}\right]^{2\ell+1}, \tag{2.3}$$

where Q=7.551 MeV is the reaction Q value for ^{13}C(p,γ_0). (In all cases, Coulomb functions were computed at a matching radius of $R_0 = 4.56$ fm.)

The direct capture ^{13}C(p,γ) contribution was taken as

$$\sigma_{\rm dc}^l(E) = \sum_S \sigma_{\rm dc}^{l,S}(E) = C^2S \times \sum_S \sigma_{\rm dc}^{\rm th}(l,S,E), \tag{2.4}$$

where C^2S is the spectroscopic factor of the final state. The theoretical l-wave DC cross section for channel-spin S, $\sigma_{\rm dc}^{\rm th}(l,S,E)$, was computed using the model of Rolfs [34] where the initial state wave functions are the usual s- or d-wave Coulomb wave functions, $U_l(kr) = \cos\delta_l F_l(kr) + \sin\delta_l G_l(kr)$, with δ_l the l-wave hard-sphere phase shift at R_0. The ^{14}N ground-state wave function was computed for an external Coulomb potential plus a square-well nuclear potential of radius R_0 whose depth was adjusted to reproduce the experimental binding energy. The resulting theoretical DC cross section was then approximated as

$$\sigma_{\rm dc}^{\rm th}(l,S,E_p) = |b(S,l)|^2 \frac{(A_l + B_l E_p + C_l E_p^2)}{E_p} \times \exp(-2\pi\eta), \tag{2.5}$$

with parameters $A_{0(2)} = 1.66\times10^{-3}(1.42\times10^{-6})$ mb keV, $B_{0(2)} = -1.37 \times 10^{-6}(7.40 \times 10^{-8})$ mb, $C_{0(2)} = 3.77 \times 10^{-10}(-1.38 \times 10^{-12})$ mb/keV. We fitted the measured $^{13}{\rm C}(p,\gamma_0)$ cross section with the expression

$$\begin{aligned} 4\pi\frac{d\sigma(E_p,90^\circ)}{d\Omega} = {} & \sum_i \sigma_r^i(E_p)W_r^i(90^\circ) + \sum_{l=0,2} \sigma_{\rm dc}^l(E_p)W_{\rm dc}^l(90^\circ) \\ & +2\sum_{i,l_{\rm dc}} \sqrt{\sigma_r^i(E_p)\sigma_{\rm dc}^{l_{\rm dc},S_i}(E_p)}\cos(\phi_i + \xi_{l_i} - \xi_{l_{\rm dc}})W_{r-{\rm dc}}^{l_i,l_{\rm dc}}(90^\circ) \\ & +2\sqrt{\sigma_{\rm dc}^0(E_p)\sigma_{\rm dc}^2(E_p)}\cos(\xi_2 - \xi_0)W_{\rm dc-dc}^{0,2}(90^\circ), \end{aligned} \tag{2.6}$$

where the resonant phase shift is

$$\phi_i = \tan^{-1}\left(\frac{\Gamma_i(E_p)}{2(E_p - E_i)}\right). \tag{2.7}$$

Note that at 90°, the *s*- and *d*-wave DC terms interfere only with the negative parity resonances listed in Table I. The resonance angular distributions are

$$W_r^i(\theta) = 1 + a_2^i P_2(\cos\theta)Q_2(\cos\theta), \tag{2.8}$$

where the angular attenuation coefficient for our detector at these γ-ray energies is $Q_2(90^\circ) = 0.88$. For $l > 0$ or $J = 0$ resonances, we took the a_2 coefficients from the literature [35–37]. The magnitudes and angular distributions of the interference terms were calculated using the expressions in Ref. [34]. However, we did not restrict ourselves to the assumption that the resonance and DC terms had the same channel-spin structure as is implicitly assumed in Ref. [34]. In Eq. (2.5), $b(S,l)$ is the fractional amplitude of the l-wave DC component with channel spin S_i (see, for example, [38]), normalized so that $\sum_S |b(S,l)|^2 = 1$.

The best fit to the data in Fig. 4 was obtained for $C^2S = 0.39$. A more detailed analysis of our $^{13}{\rm C}(p,\gamma)$ data will be presented elsewhere [39].

A. Properties of the 0_1^-;1 level

The data in Fig. 4 yield resonance energies of $E_p^{\rm lab}(0_2^+;1) = 1156 \pm 2$ keV and $E_p^{\rm lab}(0_1^-;1) = 1347 \pm 7$ keV. The observed center-of-mass width for the $0^-;1$ level, $\Gamma = 440 \pm 8$ keV, corresponds to a spectroscopic factor $S = \Gamma/\Gamma_{\rm s.p.} = 0.75$, where the single particle proton width $\Gamma_{\rm s.p.}$=588 keV was computed [40] from the expression

$$\Gamma_{\rm s.p.} = \frac{2P_l(E_r)\gamma_{\rm s.p.}^2}{1 + \gamma_{\rm s.p.}^2(dS/dE)_{E_r}}, \tag{2.9}$$

where the reduced width was

$$\gamma_{\rm s.p.}^2 = \frac{\hbar^2 a}{2\mu}\frac{\phi^2(a)}{\int_0^a \phi^2(r)r^2dr}. \tag{2.10}$$

The single-particle wave function $\phi(r)$ was evaluated in a Woods-Saxon well with standard geometry. The shift function S was summed over all channels. For the single-particle case, this corresponded to the open proton channel, $^{13}{\rm C(g.s.)} + p(2s_{1/2})$, and the closed neutron channel, $^{13}{\rm N(g.s.)} + n(2s_{1/2})$. Our value for $S(0^-)$ agrees reasonably with the value $S(0^-)$=1.02 deduced for the analog level in ^{14}C [26].

The γ-decay widths and branching ratios of the $0^-;1$ level were measured in long runs taken at three energies across the broad resonance (E_p =1.042, 1.293, and 1.633 MeV). The 0^- state was known to γ decay almost entirely by an $E1$ transition to the ^{14}N ground state. We searched for weak branches to all lower lying 1^+ and 1^- levels, but resonant yields were not observed to any other level. As the excited states to which the 0^- level might decay all subsequently decay to the 2.313 MeV level, a rough upper limit on the sum of all other branches was obtained by searching for a resonant yield of $\gamma_{2.313}$. We estimate a 3% upper limit on the sum of all other branches of the 0^- level. The estimate is necessarily rough, because the branching ratios from the various levels to the $0_1^+;1$ state vary. This value is in good agreement with recent measurements of King [41], $\Gamma_{\gamma_0}/\Gamma_\gamma = 0.969 \pm 0.010$.

Table I shows our best values for the energy and width of the $0^-;1$ level. Although different assumptions about the background and interference terms may cause these values to vary somewhat, such variations have little effect on the size of the expected PNC signal. All our fits, whether they included or omitted background terms, $l = 0/l = 2$ DC interference, or high-energy resonances, gave $0^-;1$ widths and energies that were correlated in such a way that the predicted PNC signal at the energy of our measurement was constant to within 7%.

B. Properties of the 0_2^+;1 level

The width of the $0_2^+;1$ resonance was measured with a separate excitation function from $E_p^{\rm lab}$ = 1120 to 1200 keV. Because the resonance is so narrow, a thinner target (~ 25 μg/cm^2) was used. At the energy of the $0_2^+;1$ resonance, the γ_0 yield had a substantial contribution from the $0^-;1$ resonance. We enhanced our sensitivity to the $0_2^+;1$ width by excluding the γ_0 transition and analyzing the summed γ yields to the excited states and their subsequent decay γ rays. The first panel of Fig. 5 shows an excitation function of the sum of lower energy γ yields ($\gamma_2+\gamma_5+\gamma_7+$ secondaries) across the $0^+;1$ resonance. Notice the strong background suppression compared to ^{13}C(p,γ_0) data in Fig. 4.

As the width of the $0_2^+;1$ level was comparable to the energy loss in the target, it was important to determine the target thickness precisely. The target thickness and beam energy resolution (24.3 ± 1.1 μg/cm^2 and 550 ± 100 eV, respectively) were obtained from a THICKTARGET fit to data taken over the narrow E_p = 1.75 MeV resonance (see Fig. 6). The curve in Fig. 5 is the THICKTARGET fit to the $0_2^+;1$ γ-yield assuming a single isolated resonance with a constant background, using the target and beam parameters obtained above. We infer a level width of $\Gamma_{\rm c.m.}(0_2^+;1)=4.0\pm0.3$ keV which is substantially smaller than the previously accepted value of $\Gamma_{\rm c.m.}=7\pm1$ keV. Our value for Γ corresponds to a spectroscopic factor $C^2S=0.021$, which is consistent with a nearly pure $2\hbar\omega$ configuration for the 0_2^+ level.

We determined the γ-ray branching ratios by taking long runs above, at, and below the resonance (E_p = 1.132, 1.156, and 1.176 MeV), and the "on" vs "off" resonance γ spectra were compared. The $0_2^+;1$ level γ decays predominantly via $M1$ transitions to all the lower-lying $1^+;0$ levels. Our measured ground-state branching ratio of the $0_2^+;1$ level is much smaller than the previously accepted value. The weakness of the $0_2^+;1\to1_1^+;0$ transition (Γ_{γ_0}=0.37±0.05 eV) again indicates that the 0^+ level is a nearly pure $2\hbar\omega$ 2p-4h configuration.

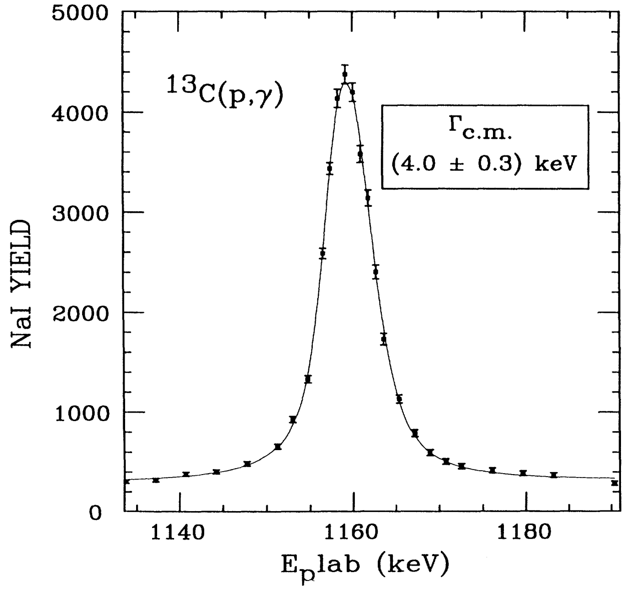

FIG. 5. Excitation function of the ^{13}C(p,γ) yield to excited states and their secondary decays across the $0_2^+;1$ resonance. The solid curve is a THICKTARGET fit using the beam energy resolution and target thickness parameters obtained from the data of Fig. 6.

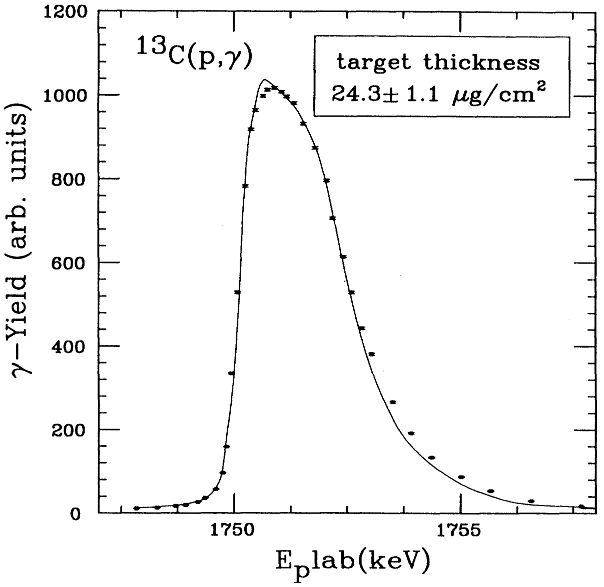

FIG. 6. Excitation function of the γ-ray yield across the 135 eV wide resonance in ^{13}C(p,γ). The solid curve is a THICKTARGET fit to the level. A target thickness of 24.3 ± 1.1 μg/cm^2 was extracted along with a beam energy spread of 550 ± 100 eV.

C. Parity-conserving ^{13}C + p reactions

An important test of the adequacy of our S-matrix formalism for analyzing A_L data is its ability to reproduce the parity-conserving features of ^{13}C + p reactions. We tested the reaction theory in two independent ways: by studying the ^{13}C(p,γ) reaction from E_p=0.45 to 3.0 MeV, and by studying the ^{13}C$(\vec{p},p)$ reaction from E_p=1.1 to 2.2 MeV.

The ^{13}C(p,γ) results have already been shown in Fig. 4. The excellent agreement between the data and the fit are evidence that our reaction model and resonance parameters gave a good account of the relevant levels of ^{14}N.

The ^{13}C$(\vec{p},p)$ data were obtained with a ~ 95% enriched 27.7 μg /cm^2 target using the apparatus (discussed below) designed for the PNC measurement. Figure 7 shows count rate and analyzing power at $\overline{\Theta}_{\rm lab}$ = 35° and $\overline{\Theta}_{\rm lab}$ = 155°. Figure 7 also shows our theoretical predictions averaged over the large detector solid angles and the finite target thickness. The resonance parameters were not adjusted to improve the fit, but were taken from Table I. The model gives a very good account of the data in the important region below E_p = 1.6 MeV and is still quite satisfactory up to E_p = 2.0 MeV. At higher energies the predictions begin to deviate more as the level structure of ^{14}N becomes more complex and less well known. While this region is not relevant to our PNC experiment, it does contain useful information about levels of ^{14}N with E_x > 9.0 MeV, so we discuss it briefly. The E_p = 1.98 and 2.11 MeV resonances, corresponding to the E_x = 9388 and E_x = 9509 keV levels of ^{14}N, are known [42] to have l = 2, and the lower resonance has

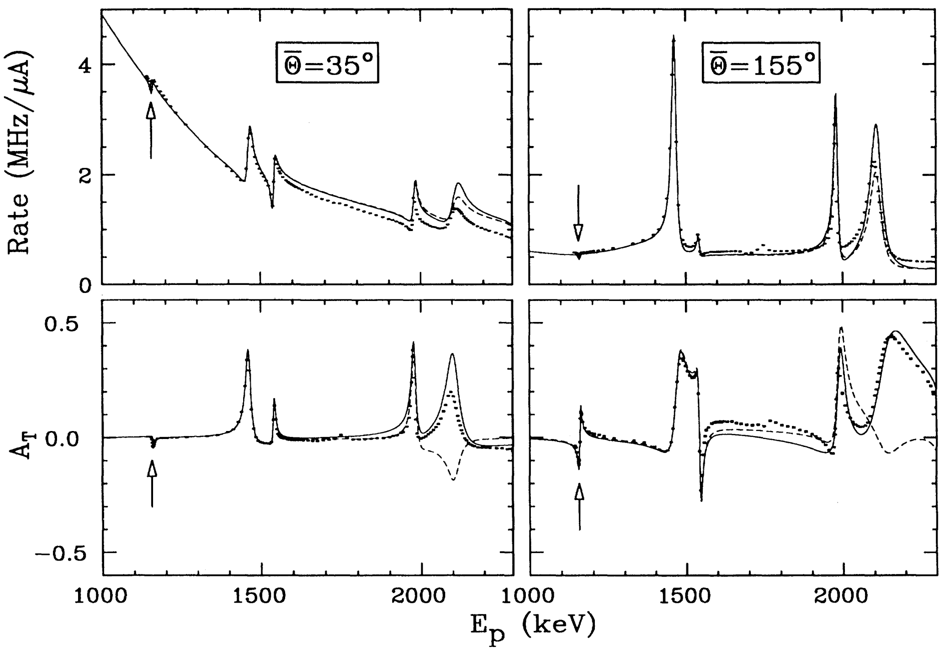

FIG. 7. $^{13}C(\vec{p},p)$ count rate and analyzing power measured using the PNC apparatus described in Sec. III. The data have been corrected for a small ^{12}C target contaminant. The small dots are the data, and the solid (dashed) line is the theoretical curve assuming an $l = 2, S = 1, J = 2$ ($l = 2, S = 1, J = 3$) assignment for the $E_p = 2.11$ MeV resonance. The arrows show the location of the resonance whose parity properties are the subject of this paper. The S-matrix theory gives a very good account of the data in the region of interest.

been assigned $J^\pi = (2,3)^-$ while the upper is thought to be $J^\pi = 2^-$ [24]. We computed count rates and analyzing powers for the four cases where either of the two resonances had $J = 2$ or $J = 3$. We found that while the assignment of $l = 2, S = 1, J = 2$ for the $E_p = 1.98$ and 2.11 MeV resonances reproduced the cross sections, it gave analyzing powers of the wrong sign. The best agreement was found for a $l = 2, S = 1, J = 3$ assignment to both levels. This reproduced the data over the $E_p = 1.98$ MeV resonance, but overpredicted the cross-section and analyzing power over the $E_p = 2.11$ MeV resonance. Thus, we strongly favor the 3^- assignment for the $E_p = 1.98$ MeV resonance. The discrepancy over the $E_p = 2.11$ MeV resonance may have arisen because this resonance is highly channel-spin mixed [42], and channel-spin mixing for the parity-conserving process was not included in our S-matrix formulation. Therefore we cannot reach a definite conclusion regarding the spin of the 2.11 MeV resonance. Fortunately, the lower energy resonances must be channel-spin eigenstates, and for these resonances our model was very successful.

The ability of our S-matrix reaction theory to account quantitatively for the $^{13}C(\vec{p},p)$ parity-conserving observables in the low-energy region of interest (see Fig. 9), supports our application of this theory to the parity-violation problem.

D. Expected parity violation in $^{13}C(\vec{p},p)$ elastic scattering

Using the formalism described in Sec. I B, and the resonance parameters determined in Secs. II A and II B, we predict that the longitudinal analyzing power has a sharp energy dependence across the 0^+ resonance, with the maximum PNC effect occurring at extreme back angles and energies near the center of the resonance. Figure 8 shows the predicted angular distribution of A_L at the maximum of the PNC effect. Assuming a weak matrix element of $\langle H_{\rm weak}\rangle = -1.04$ eV, a maximum analyzing power of $A_L^* = -3.5 \times 10^{-5}$ is expected for an infinitely thin target and detectors at extreme back angles.

III. APPARATUS

A. General considerations

1. Maximizing the statistical accuracy of the A_L measurement

Maximizing the statistical accuracy required optimizing the solid angle coverage and target thickness. It was clearly advantageous to place detectors at extreme back angles where we expected the largest PNC effect (see

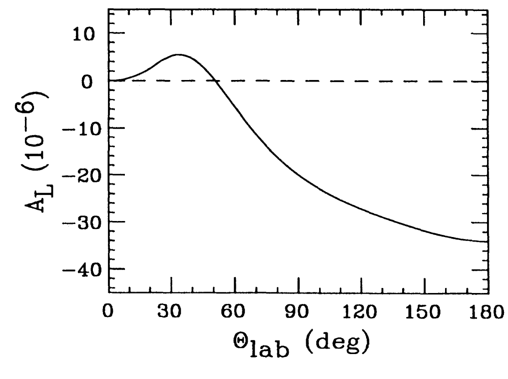

FIG. 8. Predicted angular distribution of A_L at $E_p = 1157.5$ MeV, the energy of the maximum PNC effect.

Fig. 8). Practical limitations restricted our coverage to $\approx$ 57% of the solid angle between $\Theta_{\rm lab} = 141.2°$ and $\Theta_{\rm lab} = 168.8°$. Because of the increased cross section at forward angles, comparable statistical accuracy on the PNC asymmetry could be obtained at forward angles near 35°. So we added a second set of detectors that covered about 16.5% of the solid angle between $\Theta_{\rm lab} = 29.7°$ and $\Theta_{\rm lab} = 40.3°$. By measuring the difference in the analyzing powers between the *front* and *back* detectors, we increased slightly the expected PNC signal and reduced our sensitivity to certain sources of systematic error as discussed below. Although the *front* detector solid angles could easily have been larger, the statistical accuracy of the difference asymmetry $A_L(B) - A_L(F)$ would not have increased appreciably and the system would have been more sensitive to systematic effects (see below).

The optimum PNC signal occurs for a target thickness of about 25 μg/cm^2 which gives an energy loss comparable to the 4 keV width of the 0^+ resonance. Prior to the PNC measurement, we measured the count rates and the averaged transverse analyzing powers across the 0^+ resonance with a 25 μg/cm^2 target and the same detector array (described in detail below) used in the PNC measurement. The data points, together with the angle-averaged and target-thickness-integrated predictions for the analyzing powers and count rates are shown in Fig. 9. The agreement between the predicted and measured quantities is quite good. The central panels in Fig. 9 show the corresponding angle and target-thickness averaged longitudinal analyzing power predictions assuming $\langle H_{\rm weak} \rangle = -1.04$ eV. The shaded region is a 1σ statistical error band for $IP^2 = 1$ μA day of integrated beam current, where I is the beam current and P is the longitudinal polarization of the beam. The maximum predicted PNC effects were $A_L(B) = -2.2 \times 10^{-5}$, $A_L(F) = 0.6 \times 10^{-5}$, and a signal $A_L(B) - A_L(F) = -2.8 \times 10^{-5}$. We expected a 5.1σ effect after counting for $IP^2 = 1$ μA day.

2. Minimizing the sensitivity to systematic effects

Many systematic effects result from small unwanted changes in beam properties (other than beam helicity) that correlate with spin reversal (e.g., energy, intensity, position, angle, transverse polarization components, etc.). The sensitivity to many of these systematic effects can be minimized by using detectors that are arranged symmetrically about the beam axis. Many strategies for monitoring and minimizing such effects were developed by experimenters who studied the small ($A_L \sim 10^{-7}$) longitudinal analyzing power in proton-proton scattering, particularly by the group that made very precise measurements at $E_p = 45$ MeV [5]. However, the problems we faced differed significantly from those solved in the $\vec{p} + p$ experiments. The very narrow, low-energy ^{13}C+p resonance that produces the PNC effect has a cross section with a strong energy and angle dependence and a substantial transverse analyzing power; none of these were present in the $\vec{p} + p$ experiments. Furthermore, the low beam energy ($E_p \approx 1$ MeV vs $E_p = 45$ MeV) prevented us from adopting the methods of Ref. [5] for monitoring systematic effects caused by residual transverse polarization. Therefore, we had to develop special tools to measure and control the beam energy and the residual transverse polarization.

Two effects—intensity modulation and position modulation—when coupled to target nonuniformities cannot be minimized by the symmetric detector arrangement. To the extent that the count rates depend linearly on both beam intensity and target thickness, the sensitivity to both of these effects can be dramatically reduced by forming the PNC signal from the difference of two asymmetries: $A_{\rm PNC} \equiv A_L(B) - A_L(F)$, which yields a statistical and systematic advantage over a single-angle measurement.

B. Principal components of the apparatus

1. Overview

The main features of the apparatus are shown schematically in Fig. 10. A 1.15 MeV longitudinally polarized proton beam from the University of Wisconsin EN tan-

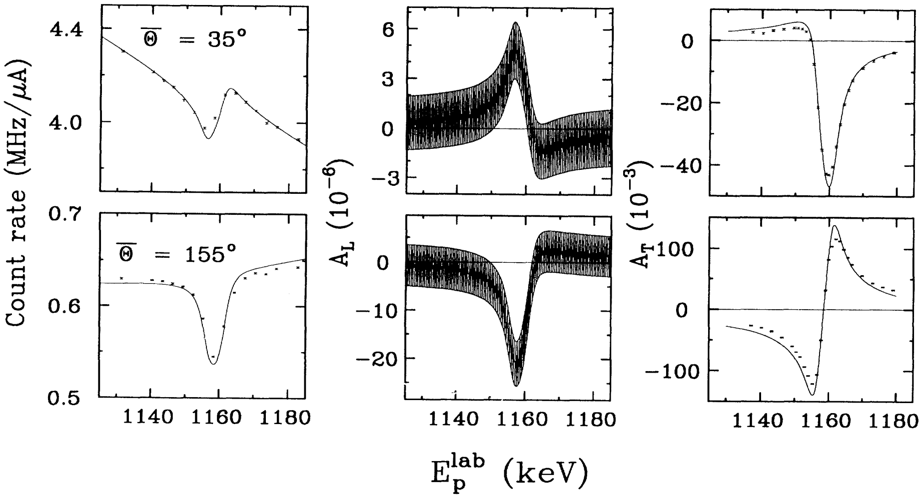

FIG. 9. ^{13}C($\vec{p}$,p) excitation function over the 0^+; $T = 1$ resonance at $E_p = 1.15$ MeV. The left panels show the count rates for the front and back detectors, the right panels show the corresponding transverse analyzing powers (A_T). The solid curves are predictions based on the S-matrix calculation averaged over target thickness and detector solid angle. The center panels show longitudinal analyzing power predictions based on the same model. The shaded area represents a 1σ statistical error band expected from 1 μA day of an integrated beam.

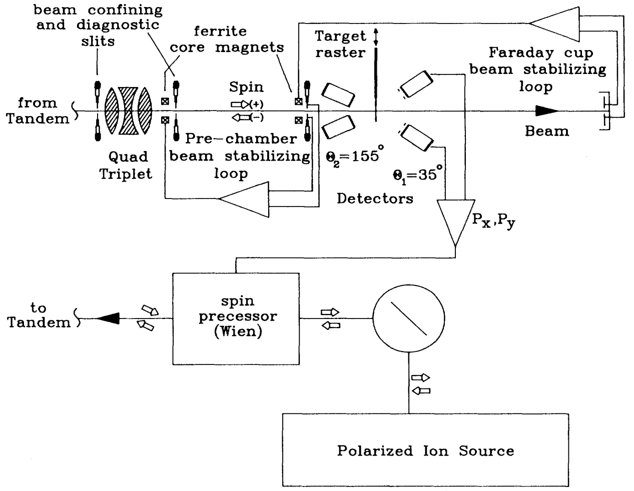

FIG. 10. Schematic of the experimental apparatus. The setup is essentially identical in both the x and y planes.

dem accelerator bombarded a $\sim 25\ \mu\mathrm{g/cm^2}$ ^{13}C target. The PNC helicity dependence of the elastic scattering cross section was measured with two sets of four-detector arrays that detected protons scattered at mean angles of $\overline{\Theta}_{\mathrm{front}} = 35°$ and $\overline{\Theta}_{\mathrm{back}} = 155°$, and at four azimuthal angles set 90° apart.

The count rates were low enough and the predicted PNC effects were large enough that individual pulses could be counted. As elastic scattering was the only particle decay channel, the detectors and subsequent signal handling could be quite simple. Protons were registered in plastic scintillators that fed discriminators whose output signals were alternately routed into two sets of scaler banks—one bank for each spin state. The spin was reversed every 20 ms so that the count rates for the two spin states were measured essentially simultaneously.

The beam axis on target was stabilized to reduce possible helicity-dependent beam axis modulations. Any transverse components of the spin were monitored by the transverse asymmetries in the scintillation detectors and then nulled by correcting the spin orientation at the ion source. The beam energy stability was monitored to high precision using the known sharp energy dependence of the transverse analyzing power over the 0^+ resonance. Finally, any target nonuniformities were smoothed out by translating the target in the plane perpendicular to beam axis in a raster pattern.

2. Detectors

The proton detectors were ~ 100-μm-thick plastic scintillators with 0.4 μm of aluminum on the front face, coupled to 5.1-cm photomultiplier tubes (PMT's). The scintillator thickness was chosen to stop 3 MeV protons while maintaining a low efficiency for γ rays. The aluminum coating reflected scintillation light back into the PMT, maximizing light collection efficiency and minimizing optical crosstalk between the detectors without appreciably degrading the proton energy.

The detectors were placed in magnetically shielded and electrically isolated vacuum mounts (see Fig. 11). The front (back) detectors, located 13.5 (9.9) cm from the target with apertures of 1.27 (4.83) cm, had solid angle coverages of $\Omega_{\mathrm{front}} = 4 \times 27.5$ msr and $\Omega_{\mathrm{back}} = 4 \times 181$ msr. With this arrangement, the front-to-back count-rate ratio was a tolerable 7:1 value, and the detector energy resolution (Fig. 12), limited by photocathode nonuniformities, was acceptable.

3. Targets

The ^{13}C foils, enriched to $> 95\%$, were commercially fabricated by electron sputtering. We selected those targets that had the fewest visible defects arising from sputtering of macroscopic particulates.

As the detectors did not resolve protons scattered by ^{13}C from those scattered by target contaminants, it was essential to maintain a good vacuum near the target, and in particular to eliminate sources of hydrocarbons that crack natural carbon onto the targets exposed to the beam. To this end, Viton O-rings were used throughout, a cryopump and sorption pump were employed, and a liquid-nitrogen trap upstream from the target isolated our apparatus from the accelerator. In addition, a large cold shroud was placed around the target to minimize the unavoidable hydrocarbon contamination from the detectors. Effects from target nonuniformities and ^{12}C buildup were reduced further by translating the target in a 3.1 mm × 3.1 mm raster pattern (by controlling the raster pattern, we could also find the most uniform area of each target). With these measures, we attained a beamline vacuum of $\sim 5 \times 10^{-8}$ Torr and a ^{12}C buildup rate of ~ 0.1 ($\mu\mathrm{g/cm^2}$)/day for a 150–200 nA beam of 1.15 MeV protons.

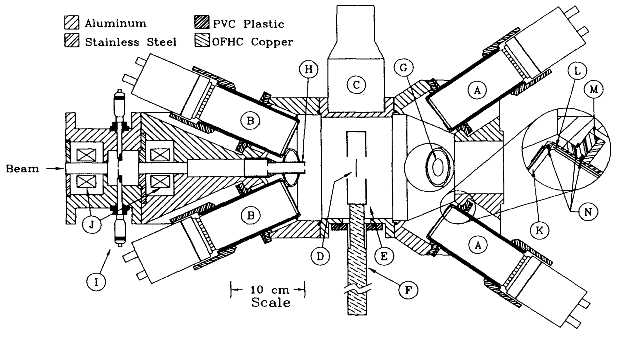

FIG. 11. Cross section of the scattering chamber cut in the vertical plane. A, front photomuliplier tube (PMT); B, back PMT; C, NaI detector; D, ^{13}C target; E, cold shroud and Faraday cup shield; F, cold finger vacuum feedthrough; G, front detector aperture; H, clean-up collimator; I, four-jaw adjustable aperture; J, steering magnets; from inset, K, Lucite-backed scintillator; L, μ-metal shield; and, M, insulator; N, O-ring seals.

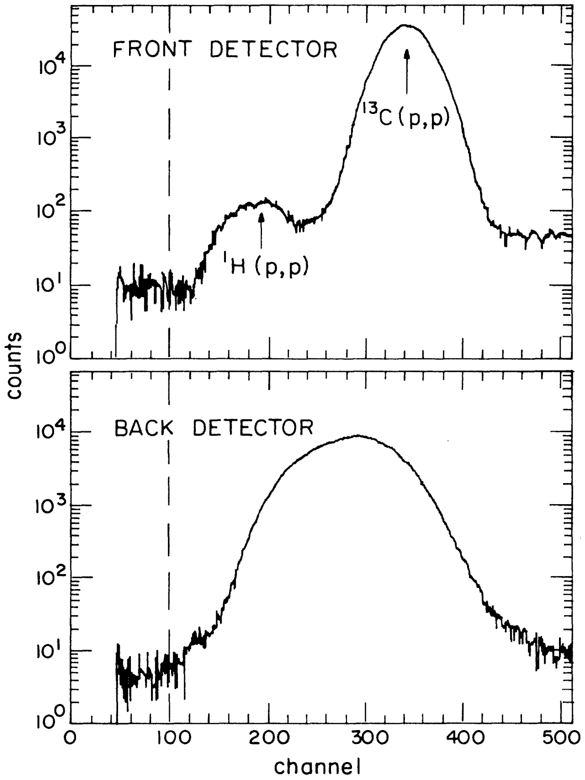

FIG. 12. Pulse-height spectra in the proton detectors under typical operating conditions.

4. Polarized ion source and beam transport

The atomic-beam polarized ion source [43] produced an H^- beam of ≈ 1 μA, and under our operating conditions gave a polarization of ≈ 0.85. The helicity of the beam was reversed by alternately energizing one of two RF cavities through which the atomic hydrogen beam passed. This allowed polarization reversal with very little change in the intensity or the emittance of the beam.

After acceleration and momentum analysis, the beam was deflected 25° onto the beamline where a quadrupole triplet formed an essentially square (1 mm × 1 mm) beam spot (the image of the momentum analysis slits). Steering elements were placed at all critical locations along the beam transport to help optimize beam transmission. As the spin direction on target was quite sensitive to the tuning of magnetic steerers at the low-energy end of the tandem, these were not adjusted after an initial tune-up.

5. Beam stabilization

The beam stabilization systems consisted of six feedback loops that controlled the position, angle, and spin direction of the beam in both transverse directions, and a conventional corona current regulator that stabilized the beam energy. A fine-tuning system for maintaining long-term beam energy stability was also required.

The beam axis was stabilized by two sets of dual feedback loops that maintained the position $(\overline{x},\overline{y})$ and angle $(\overline{\theta}_y,\overline{\theta}_x)$ at the target. (Throughout this paper we denote the beam axis by $\hat{z}$, and $\hat{y}$ is a vector pointing directly upwards from the center of the beam spot on the target.) One pair of loops used fast steerer magnets located at the exit of the beamline quadrupole triplet to stabilize the beam position at a set of adjustable four-jaw slits located 34 cm before the target. These loops predominantly stabilized the beam *position* on target, as the steering magnets were near the "belly" of the beam. A second pair of loops used fast steerer magnets located at the four-jaw slits to stabilize the beam position at the Faraday cup 177 cm downstream from the target. The Faraday cup was divided into five segments (a circular central region, and left, right, up, and down quadrants) all of which were individually monitored; the left-right and up-down differences were used as error signals in the feedback loops. The Faraday cup loops predominantly stabilized the beam *angle* on target, as their steering magnets were located near a beam focus. At low frequencies ($<$ 500 Hz), the slit loops reduced beam noise by 20 to 30 dB, while the cup loops reduced the beam noise by $\sim$ 15 dB.

The spin stabilization loop used the transverse analyzing power in the scintillation detectors to determine the transverse components of the polarization after each data *dump* ($\sim$ 20 minutes of data collection)—a counting period long enough to detect residual transverse polarizations with sufficient statistical precision. If a significant transverse polarization component was observed, the data aquisition and control computer automatically corrected the ion source spin precessor before the next *dump* began. This feedback loop was highly effective: the time-averaged net transverse polarization was typically reduced to $P_\perp A_T \approx 1 \times 10^{-5}$.

6. Data acquisition and experiment control

The data acquisition system was centered around an IBM PC/AT computer. A schematic diagram of the electronics setup is shown in Fig. 13. The PMT anode pulses fed updating discriminators with widths set to 12 ns. The discriminator outputs were sent to the counting room and reshaped by identical discriminators with widths reduced to 8 ns to ensure that the first set of discriminators dominated the system deadtime. The discriminator signals were fanned-out into two sets of CAMAC scalers, which were alternately gated off according to the spin state. Immediately after the scalers were read and cleared, the function of the scaler banks was electronically alternated by a routing switcher. This broke the correlation between spin state and scaler bank and compensated for differences in deadtimes between the individual scaler units. A test pulser fed signals into a test scaler during only one spin state to ensure routing integrity.

Currents from the Faraday cup segments and four-jaw slits were digitized and registered in another set of scaler banks. The NMR frequency of the energy analyzing magnet was measured by counting the prescaled

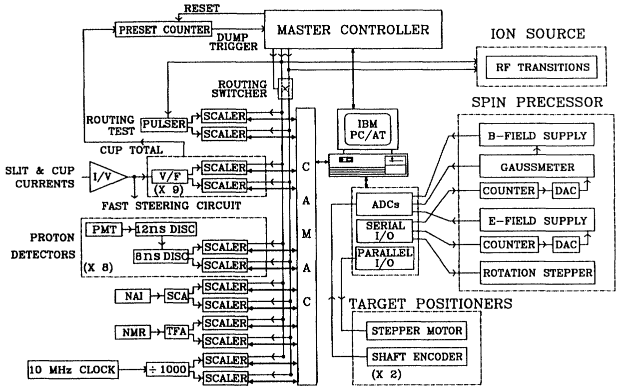

FIG. 13. Schematic diagram of the data-acquisition and experiment-control electronics.

RF of the NMR along with the output of a temperature-stabilized reference clock, which allowed us to measure the frequency to about 1 part in 10^5.

The primary function of the master controller was to define precisely the beginning and end of each data collection period (the basic unit was called a *read*). The length of a *read* was determined by a preset counter that integrated the beam current. At the beginning of each *read*, the master controller initialized the preset counter and synchronized the start of the data collection period with the beginning of a spin-flip period (20 ms with 0.5 ms gate-off). Data collection proceeded until the preset charge was accumulated, at which point the preset counter signalled the master controller. The master controller then waited until an integral number of spin-flip periods had elapsed before terminating data collection and signalling the computer to process the new data. Between each *read*, the master controller toggled the routing switcher, reversing the correlation between scaler bank and RF unit.

The crossed-field spin processor was remotely operated from the PC/AT. The computer calculated the fields required to produce a given spin orientation at the target and set the E- and B-field power supplies accordingly. The E-field power supply voltages and the output of a magnetometer that probed the B field were read back to the computer through ADC's. The spin precessor azimuthal orientation was also set by computer.

The stepper motors for the target raster mechanism were controlled by parallel output from the computer. The absolute target position was monitored with optical encoders. At the end of a *dump* (36 *reads*) the target was returned to the origin and the optical encoder values were checked by computer for possible slippage of the target position.

Data were then written on a diskette, running and cumulative asymmetries were computed, and a new *dump* was automatically begun. A contiguous series of such *dumps* taken under nominally identical conditions constituted a *run*.

IV. THE A_L MEASUREMENT

A. Signals

Various counting-rate asymmetries proved useful in the course of this work. All were defined in terms of the rate R (defined as counts per unit charge) for a particular detector element d and spin routing state $\pm$. Following the notation of Eq. (1.6) as

$$R^{\pm}(d) = R^0(d)[1 + \hat{n}_d \cdot \vec{P}^{\pm} A_T(d) + \hat{k}_{in} \cdot \vec{P}^{\pm} A_L(d)] , \tag{4.1}$$

where $R^0(d)$ is the unpolarized count rate, $\vec{r}_d$ is the vector from the center of the beam spot to the center of the detector, $\vec{n}_d = \vec{k}_{in} \times \vec{r}_d$, and A_T and A_L are averaged over the detector solid angle and target thickness (the vanishingly small A_T^* term is neglected).

The transverse analyzing power $A_T(D)$ (D represents either the front F or back B detectors) was measured, for example, with the left-right (lr) detectors and a beam polarized in the $\hat{y}$ direction:

$$A_T(D) = \frac{\mathcal{A}_t(D_{lr})}{\overline{P_y}} , \tag{4.2}$$

where $\overline{P_y} = \frac{1}{2}(P_y^+ - P_y^-)$ is the average magnitude of the transverse polarization for the two routing states. The transverse asymmetry $\mathcal{A}_t(D_{lr})$ is defined as

$$\mathcal{A}_t(D_{lr}) \equiv \frac{\mathcal{R}_t(D_{lr}) - 1}{\mathcal{R}_t(D_{lr}) + 1} , \tag{4.3}$$

with

$$\mathcal{R}_t(D_{lr}) \equiv \left[\frac{R^+(D_l) R^-(D_r)}{R^-(D_l) R^+(D_r)} \right]^{\frac{1}{2}} .$$

As the various detectors and routing states enter symmetrically in $\mathcal{R}_t$, this expression for A_T is insensitive to differences in detector efficiencies, charge asymmetries, beam misalignments, or differences in the magnitude of the polarization between the two spin states.

The longitudinal analyzing power was measured using a longitudinally polarized beam and all four detectors,

$$A_L(D) = \frac{\mathcal{A}_z(D)}{\overline{P_z}} , \tag{4.4}$$

where $\overline{P_z} = \frac{1}{2}(P_z^+ - P_z^-)$ is the average magnitude of the longitudinal polarization, and the longitudinal asymmetry $\mathcal{A}_z(D)$ is defined as

$$\mathcal{A}_z(D) \equiv \frac{\mathcal{R}_z(D) - 1}{\mathcal{R}_z(D) + 1} , \tag{4.5}$$

with

$$\mathcal{R}_z(D) \equiv \left[\frac{R^+(D_l) R^+(D_r) R^+(D_u) R^+(D_d)}{R^-(D_l) R^-(D_r) R^-(D_u) R^-(D_d)} \right]^{\frac{1}{4}} .$$

This ratio is symmetric with respect to the detectors, but is not symmetric with respect to the routing states. As this longitudinal analyzing power is sensitive to current asymmetries it was better to compare analyzing power measurements from *front* and *back* detectors by forming the ratio

$$A_L(B/F) = \frac{1}{\overline{P}_z}\frac{\mathcal{R}_z(B) - \mathcal{R}_z(F)}{\mathcal{R}_z(B) + \mathcal{R}_z(F)} \approx A_L(B) - A_L(F) \ . \tag{4.6}$$

This ratio took advantage of the full symmetry of the apparatus and provided the best signal for the A_L measurement.

It was also convenient to define a set of centering asymmetries, such as

$$\mathcal{A}_c(D_{du}) = \frac{\mathcal{R}_c(D_{du}) - 1}{\mathcal{R}_c(D_{du}) + 1} \ , \tag{4.7}$$

with

$$\mathcal{R}_c(D_{du}) = \left[\frac{R^+(D_d)R^-(D_d)}{R^-(D_u)R^+(D_u)}\right]^{\frac{1}{2}} \ .$$

These asymmetries were useful in aligning the beam axis, as the $\mathcal{A}_c$'s were quite sensitive to small displacements of the beam.

B. Experimental procedure

More than half of the run time was spent on setup and diagnostic procedures that ensured a reliable A_L measurement. The setup procedures included setting the spin precessor control constants, measuring the target thickness, optimizing the beam focus and centering the beam axis, measuring the beam polarization, setting the beam energy, and measuring the intensity and polarization profiles of the beam.

Once the setup was complete, we followed a detailed schedule that interlaced A_L measurements with crucial diagnostic procedures (e.g., checking the beam energy and polarization, and maintaining the beam along the symmetry axis of the detector system). Several times during the course of each measurement, the ionizer solenoid field was reversed to invert the correlation between the helicity on target and the state of the RF transition units of the polarized source.

All of these procedures were greatly facilitated by powerful on-line analysis routines. We could display excitation functions of any quantity (asymmetry or count rate), the values of any quantity for a series of *dumps*, the variation of any quantity with position in the raster scan, histograms of any quantity and (where applicable) the expected statistical distribution. Other routines displayed the correlations between any two quantities, used measured asymmetries to compute the Faraday cup and slit positions that centered the beam, computed the polarization in the two spin states, fitted data to determine the spin precessor control constants, etc. These routines were so useful that the final A_L given in this paper differs only slightly from the value we had from the on-line analysis.

1. Measuring the target thickness and composition

Target thicknesses were extracted by measuring the γ yield over the 135-eV-wide ^{13}C(p,γ_0) resonance at $E_p = 1.75$ MeV and comparing the observed resonance width (typically 3.7 keV) to the known energy loss rate of $dE/d(\rho x) = 0.144\pm0.005$ keV/(μg/cm^2) [44]. The target thickness uncertainty gave a negligible ($\pm5\%$) contribution to the overall error in A_L.

The only significant contaminant was ^{12}C. We had two "handles" on ϵ_{12}, the fraction of ^{12}C in our targets. At $E_p \approx 1.7$ MeV, the ^{12}C analyzing power was so large that it produced a sizable transverse asymmetry even in highly enriched ^{13}C targets, and at the energy of the PNC measurement, the back-to-front count-rate ratio, $\mathcal{B}/\mathcal{F}$, defined by

$$\mathcal{B}/\mathcal{F} \equiv \left[\frac{\prod_{\rm back} R^+(d)\prod_{\rm back} R^-(d)}{\prod_{\rm front} R^+(d)\prod_{\rm front} R^-(d)}\right]^{\frac{1}{8}} \ , \tag{4.8}$$

was quite different for the two isotopes: $\mathcal{B}/\mathcal{F}(^{12}\text{C}) \approx 2.1\mathcal{B}/\mathcal{F}(^{13}\text{C})$.

Figure 14 demonstrates the effect of ^{12}C contamination on the observed $\mathcal{B}/\mathcal{F}$ ratio. Hydrocarbons cracked onto the target caused a nearly linear increase in $\mathcal{B}/\mathcal{F}$ during the course of the measurements. A target typically began with about 3% ^{12}C; by the end of its useful life the contamination had increased to 5 or 6%. Because $\mathcal{B}/\mathcal{F}$ was sensitive to the precise $\hat{z}$ position of the target, ϵ_{12} was better determined by $A_T(F)$ at $E_p \approx 1.7$ MeV. Figure 15 illustrates this approach. We inferred ϵ_{12} from $\mathcal{A}_t(F_{du})$ using the $\Theta_{\rm lab} = 36°$ cross sections for ^{13}C and ^{12}C from Refs. [42] and [45], respectively. Run-by-run corrections for ^{12}C contamination were made by combining the two methods, allowing us to determine ϵ_{12} to better than 1% of the ^{13}C thickness.

2. Centering the beam

The symmetry axis of the detector arrays was determined before each run session. After tuning the

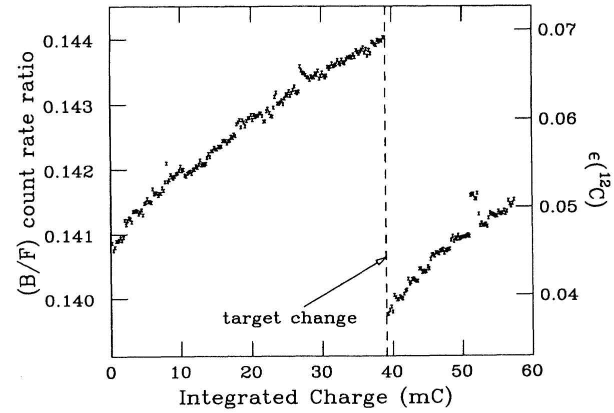

FIG. 14. The $\mathcal{B}/\mathcal{F}$ ratio as a function of integrated beam charge. The discontinuity was caused by changing to a fresh target. The scale on the right shows the deduced fraction of ^{12}C.

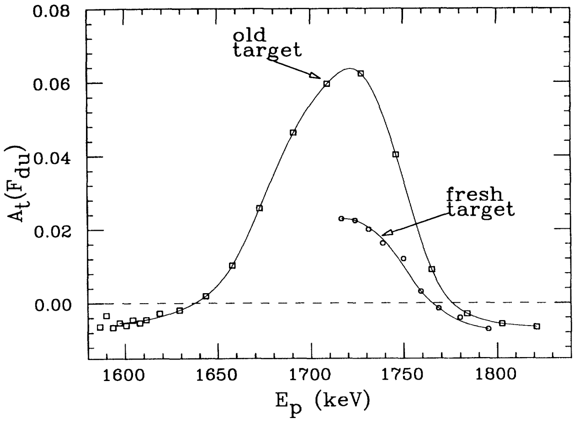

FIG. 15. Effect of the strong $^{12}C(p,p)$ resonance on $\mathcal{A}_t$'s measured with enriched ^{13}C targets. The round points are from a fresh target with a ^{12}C fraction of $\approx 3.2\%$. The square points are from a used target that contained $\approx 7.5\%$ ^{12}C. The solid line is the expectation for a pure ^{13}C target (ignoring the extremely narrow resonance at $E_p = 1.75$ MeV).

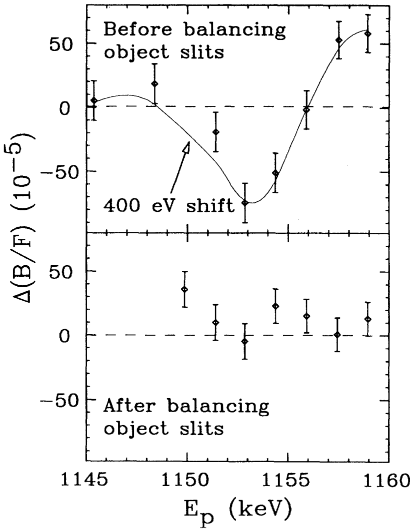

FIG. 16. $^{13}C(\vec{p},p)$ data. The vertical axis shows the difference in $\mathcal{B}/F$ for the spin longitudinal or precessed by 30°. The observed difference in the upper panel was caused by an $\approx$ 400 eV shift in the beam energy, due to residual steering in the spin precessor. The bottom panel shows that under normal conditions the energy shifted by ≤ 60 eV.

quadrupole triplet to produce the smallest beam spot, the four-jaw slits were adjusted (typically 0.8 cm gap) to intercept a small fraction (1–5 %) of the beam. The feedback loops were then energized to control of the beam position and angle on the target. The symmetry axis was determined by measuring, with a transversely polarized beam, the dependence of various asymmetries $\mathcal{A}$ on the slit (S) and Faraday cup (C) positions and fitting the results to simultaneous linear expressions

$$\mathcal{A}^F(S,C) = \mathcal{K}_S^F(S - S_0) + \mathcal{K}_C^F(C - C_0) \ , \tag{4.9}$$

$$\mathcal{A}^B(S,C) = \mathcal{K}_S^B(S - S_0) + \mathcal{K}_C^B(C - C_0) \ , \tag{4.10}$$

where S_0 and C_0 are the slit and cup positions that correspond to the symmetry axis, and the $\mathcal{K}$'s are slopes that were fitted to the data.

The selection of asymmetries for $\mathcal{A}^F$ and $\mathcal{A}^B$ was governed by the slope of the asymmetry with respect to slit and cup displacements. As the *front* detector count rate was a strong function of beam position and angle (because of the extremely sharp angular distribution), $\mathcal{A}_c(F_{du})$ and $\mathcal{A}_c(F_{lr})$ were used for $\mathcal{A}^F$. At back angles the angular distribution was so flat that small inefficiencies in the *back* counters made $\mathcal{A}_c(B_{du})$ and $\mathcal{A}_c(B_{lr})$ unreliable gauges of the symmetry axis. Therefore, the large analyzing power for the $^{12}C(\vec{p},p)$ reaction at $E_p = 1.79$ MeV, $A_T(B) = 0.83$, was used to center the beam in the *back* counters. Figure 16 illustrates how the yz-symmetry plane could be determined using a P_y polarized beam and the *up-down* detector pair. We used $\mathcal{A}_z(B_{du})$ with $\mathcal{A}_c(F_{lr})$ to determine the yz-symmetry plane, and $\mathcal{A}_z(B_{lr})$ with $\mathcal{A}_c(F_{du})$ to determine the xz-symmetry plane. This procedure determined the chamber axis to an accuracy of roughly $\Delta S_0 = \pm 0.1$ mm and $\Delta C_0 = \pm 0.4$ mm. The constants S_0 and C_0 were found to be stable over many months.

Once the detector symmetry axis was determined, the beam was "locked" to this axis by the Faraday cup and four-jaw slit stabilizing loops. However, the position of the beam centroid at the chamber slits was sensitive to the beam structure, as the slits intercepted only the "tails" of the beam. Small drifts in the beam focus would shift the centroid slightly with respect to the halo. The beam was kept on the symmetry axis by occasionally adjusting the slit positions to equalize the front counter rates. Based on the variation of the $\mathcal{A}_c$'s during the course of A_L measurements, the beam axis alignment was maintained to better than 0.2 mm and 0.6 mrad.

3. Measuring the beam polarization

The beam polarization was determined by bombarding a 50 μg/cm^2 ^{12}C target at $E_p = 1.80$ MeV, where $A_T(B) = 0.83$. This secondary polarization standard was calibrated against the known $A_T = 1$ point in the $^4He(\vec{p},p)$ reaction at $E_p = 1.75$ MeV and $\Theta_{\text{lab}} = 73°$ [46]. We measured the absolute polarization on a daily basis, or whenever gross changes in the experiment operation were necessary. Rough checks of the polarization were obtained on a 2-hour time scale using the runs where the spin was precessed 30° from longitudinal (see below), as the *front* detectors had a small analyzing power $[A_T(F) \approx 0.04]$ at the energy of the A_L measurement. The magnitude of the polarization changed by $< 2\%$ over 2-week periods, with average polarizations in the range $0.82 < |P| < 0.88$ for the run periods.

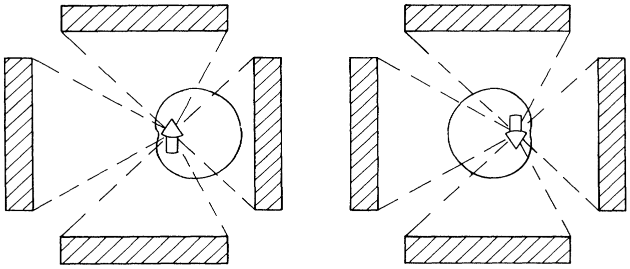

FIG. 17. Illustration of the yz-symmetry plane determination using the *up-down* detector pair in conjunction with a P_y-polarized beam. The dashed lines show the detector acceptances, the solid cardioids show the scattering intensity as a function of the azimuthal angle for the two polarization states. For small x, $\mathcal{A}_z^{ud}(B) \approx (x/r \sin\theta_B)\overline{P}_y A_T(B)$, where r is the distance from the target to the detector, and $\theta_B = 155°$.

4. Setting the beam energy

The A_L measurements were made at several energies across the 0^+ resonance. Because of the narrow width of the resonance, it was essential that the beam energy be well controlled. This could only be done by using the 0^+ resonance itself. As may be seen in Fig. 9, the strong and nearly linear dependence of $A_T(B)$ on the beam energy provided a very sensitive way to find the center of the resonance. The energy was determined by periodically precessing the spin 30° away from longitudinal and measuring $A_T(B)$ and $A_T(F)$. The spin was rotated by only 30° to minimize variations in emittance due to changing the precessor fields. We verified that the 30° spin precession introduced a beam energy shift of no more than 60 eV (see Fig. 17).

The energy was measured at the beginning and end of each series of runs (about 2 hours). The distribution of $A_T(B)$'s measured at the beginning of each series of runs corresponded to a range in energies of $\Delta E \approx 115$ eV FWHM, while the corresponding range in energies measured at the end was $\Delta E \approx 280$ eV FWHM, indicating that beam energy drifted on average by less than 200 eV during the 2-hour measurements.

C. Results

1. Summary of measurements

The A_L measurement was carried out during three 2-week periods: November 1986, February 1987, and September 1987 (see Table III).

In the first period, A_L was measured at E_p = 1158.5 keV, the energy where $A_T(B) = 0$. A single target was bombarded with a charge of 26 mC at an average beam intensity of 170 nA. About every 12 hours, the energy was raised to E_p = 1.80 MeV to determine the polarization, and to measure the transverse polarization distribution in the beam. It was not practical to measure the polarization distribution at $E_p \approx 1160$ keV because there is no good target that gives a large value of A_T at this energy.

Before the second running period, we discovered that the transverse polarization distribution varied sufficiently with energy that polarization distribution measurements at the higher energy could not be used reliably to correct the A_L results at $E_p \approx 1160$ keV. Consequently, we no longer repeatedly checked the transverse polarization distribution. Instead we simply made transverse polarization scans at the beginning of the run to confirm the rough magnitude of the polarization distributions. After a detailed analysis of the energy dependence of the sensitivity to various systematic effects (see Sec. V), we took A_L data at the energy where $A_T(B) = 0.015$, the so-called "magic energy" at $E_{\text{magic}} = 1159$ keV.

During the February 1987 and September 1987 runs, we took A_L measurements not only at E_{magic} but also (with poorer statistics) at $E_{\text{magic}} \pm 1.8$ keV and $E_{\text{magic}} +$ 4.5 keV, nearly half of the total data collection time being spent away from E_{magic}. The measurements at these other energies were primarily used to demonstrate that the systematic effects, many of which had a strong energy dependence, were not larger than expected.

In the February 1987 runs, two targets were bombarded with a charge of 31 mC at an average current of 150 nA. In the September 1987 runs, three targets were bombarded with a charge of 50 mC at an average current of 200 nA. Two of the targets used in the September runs were from the same slide, differing in thickness by < 3%, and were analyzed as one target.

TABLE III. Summary of A_L measurements at or near E_{magic}.

Run period	ρx[a] (μg/cm^2)	$\overline{E_p}$[b] (keV)	$\overline{\epsilon_{12}}$ (%)	$\overline{P_z}$	$\mathcal{A}_z(B/F)$[c] (10^{-6})	$A_L(B/F)$ (10^{-6})	$\langle H_{\text{weak}}\rangle$ (eV)
November 1986							
	27.7±1.4	1155.79±0.10	6.3±1.0	0.862±0.010	5.6±9.3	3.7±11.9 ± 3.7	0.17±0.54 ± 0.14
February 1987							
	24.0±1.2	1156.04±0.08	5.8±1.0	0.855±0.010	15.1±10.8	18.9±13.5 ± 1.7	0.82±0.59 ± 0.07
	21.2±1.1	1156.03±0.07	4.5±1.0	0.855±0.010	−0.8±16.8	−1.2±20.5 ± 1.6	−0.05±0.81 ± 0.07
September 1987							
	26.2±1.3	1156.06±0.08	3.6±1.0	0.831±0.010	3.9±7.3	5.1±9.3 ± 1.7	0.22±0.41 ± 0.07
	19.7±1.0	1156.04±0.04	4.8±1.0	0.820±0.010	27.5±21.7	42.0±28.4 ± 1.4	1.61±1.09 ± 0.06
						Final result:	0.38±0.26 ± 0.09

[a] Target thickness.

[b] $\overline{E_p}$ is the mean proton energy in the target assuming a resonance energy of 1156.0 keV.

[c] Raw asymmetry not corrected for ^{12}C contamination.

2. *Analysis*

Table III summarizes the operating conditions and results of the 826 *dumps* used to measure A_L near $E_{\rm magic}$.

We started the analysis with a simple check on the consistency of the data summarized in Table IV. For this test, we summed the counts from all the *dumps* at or near $E_{\rm magic}$ without making any corrections for variations in target thickness, beam energy or polarization, and formed a grand cumulative asymmetry, $\mathcal{A}_z^{\rm grand}(\mathcal{B}/\mathcal{F})$. This grand asymmetry and its statistical error $(6.47 \pm 4.74) \times 10^{-6}$ were then compared to the weighted mean and the standard deviation of the mean, of the 826 uncorrected $\mathcal{A}_z$'s from the individual *dumps*: $\mathcal{A}_z^{\rm mean}(\mathcal{B}/\mathcal{F}) = (6.43 \pm 5.17) \times 10^{-6}$ $[\chi^2/\nu = 1.090$, $P(> \chi^2, \nu) = 0.041]$. Figure 18 displays the distribution of all the individual asymmetries, measured at or near $E_{\rm magic}$. The excellent agreement between these two ways of computing the asymmetry, and the reasonable value of χ^2, demonstrated that the run-by-run variations in the data were almost entirely statistical, and that additional uncertainities from uncorrelated systematic effects were quite small.

After accounting for the incomplete polarization ($\overline{P_z} \approx 0.85$) a rough value for the analyzing power was obtained: $A_L(\mathcal{B}/\mathcal{F}) \approx (7.6 \pm 5.6) \times 10^{-6}$. This crude result was already in strong disagreement with the predicted effect of $A_L(\mathcal{B}/\mathcal{F}) = -22 \times 10^{-6}$.

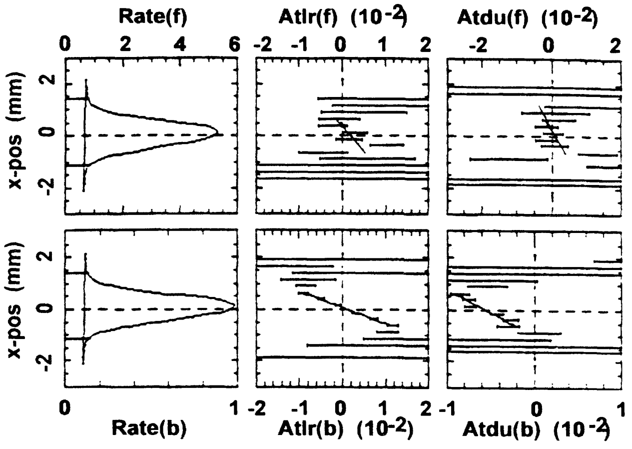

FIG. 18. Results of a strip-target scan taken directly from our on-line data analysis program. The program also calculated the beam width and slopes of the various asymmetries with respect to strip-target position.

Several small corrections were needed before a final value for A_L could be obtained. For this more refined analysis, the A_L measurements on each target were analyzed separately and the asymmetries were weighted according to the target thickness and energy of the measurement, with corrections for ^{12}C contamination and incomplete polarization. As we did not resolve protons scattered from ^{12}C and ^{13}C, the PNC asymmetries were diluted by the ^{12}C contamination [we assumed that PNC effects in ^{12}C(p,p) are negligible as there is no near degeneracy of opposite parity levels]. The $\mathcal{A}_z$'s from the *front* and *back* detectors were corrected separately according to

$$\mathcal{A}_z'(D) = \mathcal{A}_z(D)(1 + \epsilon_{12} r_D) \ , \qquad (4.11)$$

where ϵ_{12} is the fractional contamination of ^{12}C computed in Sec. IV B 1, and r_D is the ratio of ^{12}C/^{13}C cross sections for detector D. We established $r_F \approx 0.89$ by comparing ^{13}C(p,p) data of Latorre and Armstrong [42] with ^{12}C$(\vec{p},p)$ data we took at Wisconsin [45]. We determined r_B from the $\mathcal{B}/\mathcal{F}$ ratios observed with $^{\rm nat}$C and enriched ^{13}C targets, namely

$$r_B \approx \frac{\mathcal{B}/\mathcal{F}(^{\rm nat}{\rm C})}{\mathcal{B}/\mathcal{F}(^{13}{\rm C})} r_F \approx 1.91 \ . \qquad (4.12)$$

Corrections for ^{12}C contamination typically increased the observed longitudinal asymmetries in the front and back detectors by about 5% and 9% respectively. These corrections were less than 15% of the statistical error in the A_L measurements.

We express our final value for A_L as

$$A_L^* = (13 \pm 9 \pm 3) \times 10^{-6} \ , \qquad (4.13)$$

where the first error is statistical and the second is systematic (to be discussed in Sec. V). The quantity A_L^* is the maximum asymmetry one would observe with an infinitely thin ^{13}C target viewed by a counter at $\Theta = 180°$.

D. Extraction of $\langle H_{\rm weak} \rangle$

Our final results are shown in Fig. 19. The points at the three auxiliary energies (diamonds) are distinguished from the points near $E_{\rm magic}$ (boxes). The results have been scaled to a nominal target thickness of 25 μg/cm^2, and combined to form one overall analyzing power measurement for each energy. The hatched region is the "worst case" systematic error band discussed in Sec. V.

TABLE IV. Results from the simple analysis of A_L measurements.

$E - E_{\rm magic}$ (keV)	N_d	$\overline{P_z}$	$\mathcal{A}_z(\mathcal{B}/\mathcal{F})$ (10^{-6})	$A_L(\mathcal{B}/\mathcal{F})$ (10^{-6})	$\chi^2/(N_d-1)$	$P(>\chi^2, N_d-1)$
$-0.1^{\rm a}$	826	0.85±0.01	6.4±4.7	7.6±5.6 ± 1.5	1.090	0.041
−1.8	149	0.84±0.01	5±11	6±13 ± 9	1.052	0.32
+1.8	156	0.84±0.01	−4±11	−5±13 ± 7	0.965	0.65
+4.5	144	0.84±0.01	−14±11	−17±13 ± 10	1.145	0.014

[a]The measurements near $E_{\rm magic}$ are counted as one energy in this simple analysis.

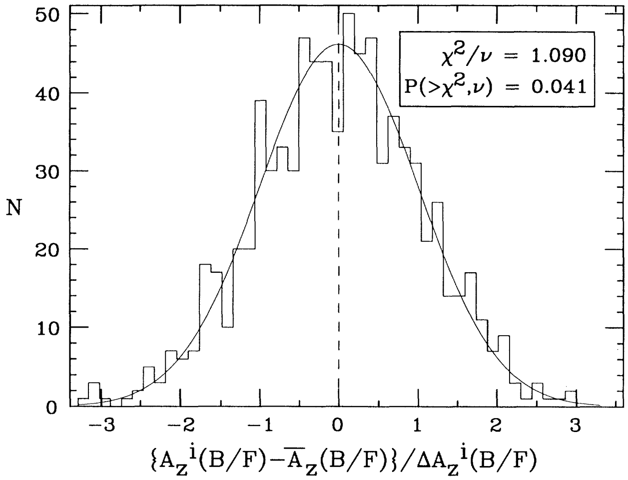

FIG. 19. Distribution of all $\mathcal{A}_z^i(B/F)$ measurements made at or near E_0. $\overline{\mathcal{A}_z(B/F)}$ is the weighted average of the measurements. A total of 862 *dumps* were accumulated, with typical statistical precisions of 1.3×10^{-4}. The solid curve is the normal distribution whose integral is 862.

The weak matrix element $\langle H_{\text{weak}} \rangle$ was inferred from the A_L measurements, after accounting for the target thickness and the predicted energy dependence of the longitudinal analyzing power. The combined result for $\langle H_{\text{weak}} \rangle$ is listed on the bottom of Table III along with the statistical and systematic uncertainties; the systematic error is the weighted average of the systematic uncertainty for each target. A ±12% scale factor error from uncertainties in the level parameters of the $J = 0$ doublet is not included in the quoted error. Our final value for the weak matrix element,

$$\langle H_{\text{weak}} \rangle = 0.38 \pm 0.26 \pm 0.09 \text{ eV} , \tag{4.14}$$

is in strong disagreement with the predictions [23], $\langle H_{\text{weak}} \rangle = -1.39$ and -1.04 eV, that were available when the experiment was begun. The experimental result is discussed further below.

V. SYSTEMATIC ERRORS

A. Overview

We aimed to place upper limits on false asymmetries that were sufficiently far below the expected PNC signal of $A_L(B/F) \sim -2.8 \times 10^{-5}$ that systematic corrections would not be needed. False asymmetries are best understood by considering the form of the PNC signal:

$$\mathcal{A}_z(B/F) = \frac{(\mathcal{B}^+/\mathcal{F}^+ - \mathcal{B}^-/\mathcal{F}^-)}{(\mathcal{B}^+/\mathcal{F}^+ + \mathcal{B}^-/\mathcal{F}^-)} = \frac{\Delta(\mathcal{B}/\mathcal{F})}{2(\overline{\mathcal{B}/\mathcal{F}})}, \tag{5.1}$$

where $\mathcal{B}^\pm$ and $\mathcal{F}^\pm$ are the mean back and front count rates for the + and − routes, $\Delta(\mathcal{B}/\mathcal{F}) = (\mathcal{B}^+/\mathcal{F}^+ - \mathcal{B}^-/\mathcal{F}^-)$ and $\overline{\mathcal{B}/\mathcal{F}} = \frac{1}{2}(\mathcal{B}^+/\mathcal{F}^+ + \mathcal{B}^-/\mathcal{F}^-)$. Any systematic effect that causes $\Delta(\mathcal{B}/\mathcal{F}) \neq 0$ generates a false asymmetry. $\mathcal{A}_z(B/F)$ may be decomposed explicitly into real and false effects:

$$\mathcal{A}_z(B/F) = \overline{P_z} A_L(B/F) + \sum_\beta S_\beta \Delta\beta + \mathcal{A}_z^{\text{elec}}, \tag{5.2}$$

where $\Delta\beta = (\beta^+ - \beta^-)$ is the difference in the βth beam parameter between spin states,

$$S_\beta \equiv \frac{1}{2\overline{\mathcal{B}/\mathcal{F}}} \frac{\partial(\mathcal{B}/\mathcal{F})}{\partial\beta} \tag{5.3}$$

is the corresponding sensitivity, and $\mathcal{A}_z^{\text{elec}}$ is a possible asymmetry in the electronics. Before the A_L measurement was made, the β's were identified, the corresponding sensitivities S_β and driving terms $\Delta\beta$ measured, and $\mathcal{A}_z^{\text{elec}}$ was shown to be negligible. We have not included an asymmetry associated with background events, as there is no background (e.g., polarized β emitters) that can produce a PNC asymmetry with this proton beam.

In general, the S_β's depend on the energy, position, and angle of the beam, and nearly all of the S_β's have a beam condition for which the sensitivity crosses through zero. For example, the sensitivity to energy modulation S_E depends on the derivative of the count rate with energy, which is strongly energy dependent and passes through zero around $E_p \approx 1159$ keV (see Fig. 20). Fortunately, two other important systematic effects—spin-angle and spin-position correlation (see Sec. V D)—have similar energy dependences with zero crossings within 100 eV of the energy-modulation zero crossing (see Fig. 21). At the mean energy of these zero crossings, the sensitivity to these potentially harmful systematic effects is reduced by about an order of magnitude compared to the sensitivities at the energy of the maximum PNC signal, while the sensitivity to the PNC effect is diminished by only 15%. Because of this fortuitous circumstance, we denoted this optimum energy for the A_L measurement as E_{magic}. Based on the measurements described below, at E_{magic} we set limits of $\mathcal{A}_z^{\text{false}}(B/F) < 2 \times 10^{-6}$, which is less than one-tenth of the expected PNC signal. The ensuing discussion summarizes these measurements; the results are tabulated in Table VII.

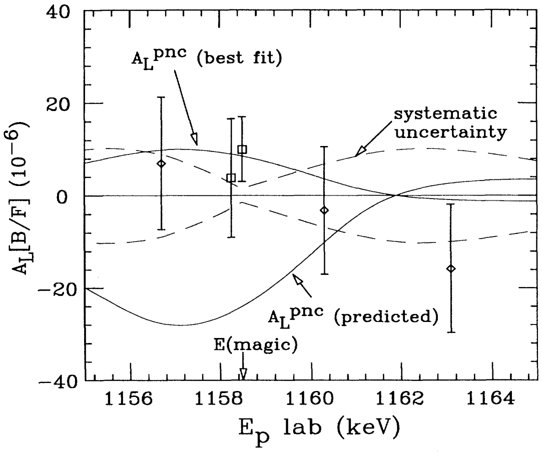

FIG. 20. Final results for the $A_L(B/F)$ measurements.

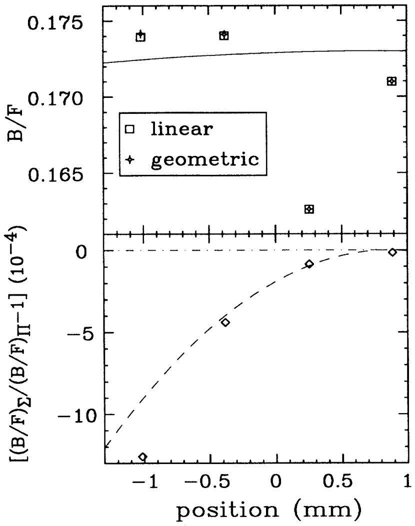

FIG. 21. The upper plot shows the dependence of $\mathcal{B}/\mathcal{F}$ on the beam displacement Δx for linear $(\mathcal{B}/\mathcal{F})_\Sigma$ and geometric $(\mathcal{B}/\mathcal{F})_\Pi$ averaging. The data were obtained using a ${}^{\text{nat}}$C target with a nonuniformity much larger than those of our ^{13}C targets. The big drop in $\mathcal{B}/\mathcal{F}$ at $\Delta x = 0.2$ mm results from this nonuniformity. The two averaging methods (crosses=geometric, boxes=linear) are nearly indistinguishable. The solid line shows the computed solid-angle effect. The lower plot shows that $[(\mathcal{B}/\mathcal{F})_\Sigma/(\mathcal{B}/\mathcal{F})_\Pi]$ was a smooth function of Δx, and that target thickness variations canceled. The dashed line is our computer model prediction.

B. Diagnostic tools

1. Computer model of detector response

We developed a computer model of the detector response that calculated the expected count rates for a given set of beam parameters and target thickness. The model incorporated simple geometric effects along with the predicted angular distribution and energy dependence of the cross section and analyzing powers. Whenever possible, we tested our understanding of the detector response by comparing the measured sensitivities to the model predictions. As will be shown, we found good agreement for all calculable effects that could contribute significantly to the experimental error.

2. Beam intensity and polarization monitor

Many systematic effects depend on the distribution of intensity and transverse polarization within the beam. These were studied using horizontal (vertical) ^{12}C strip targets that could be placed at the target position and driven vertically (horizontally) through the beam with our target translator. The scattered protons were recorded by our detectors as a function of target position. The 0.6-mm-wide strips were made by evaporating ~ 100 μg/cm^2 of carbon onto masked 2 μg/cm^2 carbon backings. Because of the high detection efficiency of our counters and the large A_T of the ${}^{12}\text{C}+p$ resonances at E_p=1.80 MeV, we could, after subtracting the background rate due to the backing, determine the spin and spatial structure of the beam from the position dependence of the rates and asymmetries (see Fig. 22). The angular structure of the beam was studied by occluding portions of the beam at the exit of the last beamline quadrupole, and observing its effect on protons scattered from a flat ^{12}C target.

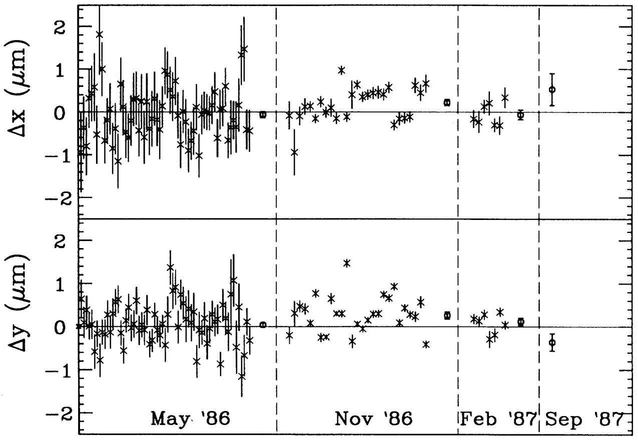

FIG. 22. Position-modulation measurements taken during the PNC and test runs. The points with crosses and unflagged error bars are the measurements; the points with boxes and flagged error bars are the average values for that run session.

C. Spin-independent effects

Spin-independent effects arise from modulations of the beam phase space that correlate with its helicity. We consider intensity, transverse phase-space (mean position and angle, and spread in position and angle), and longitudinal phase-space (energy and energy spread) modulations. Although only energy modulation and position modulation contributed significantly to our final systematic error, we estimate below the systematic errors associated with each of the above effects.

1. Intensity modulation

Atomic beam polarized ion sources that ionize in a strong magnetic field necessarily have a small intensity modulation that can be traced to the interaction energy between the atomic magnetic dipole moment and the ionizer solenoid B field [5]. This small energy difference between states produces a H^0 density difference in the ionization region, generating a beam intensity modulation of $\mathcal{A}_z(I) \approx 5 \times 10^{-5}$. Intensity variations lead to changes in the deadtime and gain of the detectors. If $\mathcal{B} \approx \mathcal{F}$ deadtime would not affect $\mathcal{A}_z(\mathcal{B}/\mathcal{F})$. Therefore, we originally used detector apertures that gave roughly equal counting rates in the front and back detectors. After finding that intensity modulation effects were negligible we enlarged the apertures on the front detectors, for a ratio of $\mathcal{B}/\mathcal{F} \approx 0.145$, to increase the statistical power of the experiment.

We measured the sensitivity to intensity modulation by varying the current in the sextupole that focused the atomic beam into the ionization region of the ion source. Because of the large inductance of the sextupole coils, this had to be done so slowly ($\approx$1 Hz) that the tandem ($\tau_{\mathrm{terminal}} \approx 10$ ms) could respond to the changing beam loading by changing its energy. We measured a $\Delta E = 16 \pm 4$ eV shift resulting from this slow flipping technique, using the $^{27}\mathrm{Al}(p,p)$ reaction discussed below. Nonetheless, the results of this test were encouraging. An intensity modulation of $\mathcal{A}_z(I) = 4.7 \times 10^{-2}$ with a beam intensity of 200 nA on a $\sim 50\ \mu\mathrm{g/cm}^2$ $^{\mathrm{nat}}$C target ($\mathcal{F} = 7.6$ MHz/μA, $\mathcal{B} = 3.2$ MHz/μA) produced an asymmetry of $\mathcal{A}_z(\mathcal{B}/F) = 2.03 \pm 0.35 \times 10^{-4}$, most of which could be accounted for by deadtime. The remainder was more likely due to induced energy modulation than to gain shifts as the discriminator rates were insensitive to small gain shifts ($S_{\mathrm{gain\ shift}} \ll 1 \times 10^{-6}$/nA) because the vast majority of pulses were well above the discriminator threshold. When scaled down to current asymmetries [$\mathcal{A}_z(I) < 1 \times 10^{-4}$] and counting rates ($\mathcal{F} \approx 3.2$ MHz/μA, $\mathcal{B} \approx 0.5$ MHz/μA) typical of our A_L measurements, the false asymmetry was negligible [$\mathcal{A}_z^{\Delta I}(\mathcal{B}/F) < 3 \times 10^{-7}$].

2. Transverse phase-space modulation

A beam-axis shift would affect not only the detector solid angles but also the region of the target that was bombarded. The symmetry of the detector array minimized the sensitivity to solid-angle changes. To the extent that the count rates were proportional to the target thickness, $\mathcal{B}/\mathcal{F}$ was also insensitive to target nonuniformities. Nevertheless, target nonuniformities dominated the sensitivity to phase-space modulations.

The sensitivities to position and angle modulations are functions of the displacement of the beam from the symmetry axis of the apparatus:

$$S_{\Delta x} = \frac{1}{2\mathcal{B}/\mathcal{F}}\left[\frac{\partial^2 \mathcal{B}/\mathcal{F}}{\partial x^2}x + \frac{\partial^2 \mathcal{B}/\mathcal{F}}{\partial x \partial \theta_y}\theta_y\right] + S_{\mathrm{tgt}}, \qquad (5.4)$$

$$S_{\Delta \theta_y} = \frac{1}{2\mathcal{B}/\mathcal{F}}\left[\frac{\partial^2 \mathcal{B}/\mathcal{F}}{\partial \theta_y^2}\theta_y + \frac{\partial^2 \mathcal{B}/\mathcal{F}}{\partial x \partial \theta_y}x\right], \qquad (5.5)$$

where the first terms in each expression represent solid-angle effects and S_{tgt} represents the additional contribution from target nonuniformities.

Solid angle effects were calculated using our computer model, as target nonuniformities made it difficult to measure these second-order effects. The computer model exactly reproduced the first-order centering asymmetries. We checked that the second-order effects were also calculated properly by comparing the $\mathcal{B}/\mathcal{F}$ ratios for linear and geometric rate averaging. These two averaging methods give different results as functions of beam displacement. The ratio $(\mathcal{B}/\mathcal{F}_{\mathrm{arith}})/(\mathcal{B}/\mathcal{F}_{\mathrm{geom}})$ is sensitive primarily to second-order geometrical effects as target nonuniformities cancel. The good agreement between the model and the data (see Fig. 23) gave us confidence in the calculated sensitivities to all geometrical effects.

The position modulation Δx was measured using strip-target scans. For a Gaussian beam distribution, the dependence of the count rate asymmetry on strip position is $\mathcal{A}_z^{\Delta x} \approx -x_s \Delta x / 2\sigma_x^2$, where x_s is the strip-target position, and σ_x is the beam width. Δx was inferred from the derivative of the count-rate asymmetry with respect to the strip position. The position modulations obtained from strip-target measurements during test and PNC runs are shown in Fig. 24. There

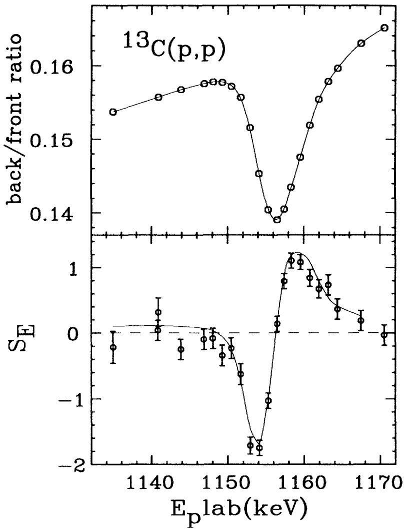

FIG. 23. Excitation functions of $\mathcal{B}/\mathcal{F}$ (panel 1) and energy-modulation sensitivity (panel 2) across the 0^+ resonance. The curve in panel 2 is the predicted sensitivity based on the derivative of $\mathcal{B}/\mathcal{F}$ of panel 1.

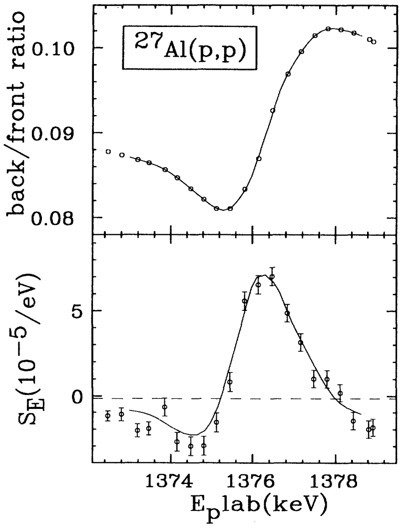

FIG. 24. $^{27}\mathrm{Al}(p,p)$ $\mathcal{B}/\mathcal{F}$ ratio and energy modulation sensitivity plotted vs E_p. The maximum sensitivity is $\partial \mathcal{A}_z(\mathcal{B}/F)/\partial E \sim 9 \times 10^{-5}$ eV^{-1}.

was clear evidence for position modulation that varied as a function of time. As we could not monitor position modulation continuously, we did not make corrections to the PNC data. Instead, we estimated an upper limit, $\Delta x, \Delta y \leq 0.36$ μm, based on the average of all the position modulation measurements ($\Delta x = 0.17 \pm 0.08$ μm, $\Delta y = 0.18 \pm 0.09$ μm) plus two standard deviations. The angle modulation $\Delta\theta$ was inferred from the Faraday cup transverse asymmetries, which had a measured response of $\mathcal{A}_t(C)/\Delta\theta \approx 4 \times 10^{-2}$ mrad^{-1}. The largest transverse cup asymmetry observed in the A_L measurements was $\mathcal{A}_t(C) = 2 \times 10^{-5}$ which corresponded to an upper limit on angle modulation of $\Delta\theta_x$, $\Delta\theta_y < 5 \times 10^{-4}$ mrad. Combining the calculated curvatures of $\partial^2(\mathcal{B}/\mathcal{F})/\partial x^2 = -9.0 \times 10^{-5}$ mm^{-2}, $\partial^2(\mathcal{B}/\mathcal{F})/\partial\theta_y^2 = -1.1 \times 10^{-5}$ mrad^{-2}, and $\partial^2(\mathcal{B}/\mathcal{F})/\partial x \partial\theta_y = -3.1 \times 10^{-5}$ mrad^{-1} mm^{-1}, with the upper limit displacements 0.1 mm and 0.6 mrad, we estimate that false asymmetries from geometrical effects of position and angle modulations are $\mathcal{A}_z^{\Delta x}(B/F) < 5 \times 10^{-8}$ and $\mathcal{A}_z^{\Delta\theta}(B/F) < 3 \times 10^{-8}$, respectively. Similar techniques yielded the beam width ($\Delta\sigma_x$) and angle spread ($\Delta\sigma_\theta$) modulations. The observed modulations corresponded to extremely small false asymmetries; the results are summarized in Table VII.

Target thickness nonuniformities presented a much larger potential for systematic error. The target was rastered in a 6 × 6 square matrix of side length Δx_{raster}=3.1 mm, allowing us to measure and reduce the sensitivity to target nonuniformities. As the beam spot size was substantially larger (1 mm×1 mm) than the target position spacings, the linear approximation could be used, yielding

$$S_{\text{tgt}} = \frac{1}{2\mathcal{B}/\mathcal{F}} \frac{\Delta(\mathcal{B}/\mathcal{F})}{\Delta x_{\text{raster}}} \; , \tag{5.6}$$

where $\Delta(\mathcal{B}/\mathcal{F})$ is the difference in the back-to-front ratio between the two edges of the raster pattern. Table V shows the sensitivities for each of the targets used in the A_L measurement. The "worst case" $\mathcal{A}_z$ is based on the upper limits on beam modulations discussed above. In all cases, the systematic uncertainty from target nonuniformities was acceptably small.

We therefore conclude that false asymmetries from any of the possible transverse phase-space modulations were small compared to the PNC signal.

3. Energy modulation

The energy-modulation sensitivity S_E was determined from an excitation function across the 0^+ resonance obtained while the target voltage was modulated to produce a 200 eV beam energy difference between the two routes (see Fig. 20). At the energy of the maximum PNC effect, $S_E = 1.5 \times 10^{-5}$ eV^{-1}, so that an acceptably small systematic error required an energy modulation below 0.2 eV.

We first attempted to set limits on energy modulation [47] by exploiting the narrow ($\Gamma = 135$ eV) ^{13}C(p,γ) resonance at $E_p = 1.75$ MeV. The energy of a longitudinally polarized beam was set on the rising edge of this resonance, and an energy-modulation sensitivity of $(1/2R_\gamma)\partial R_\gamma/\partial E \simeq 3 \times 10^{-3}$ eV^{-1} was achieved, where R_γ is the γ yield in a NaI detector. Even though this is one of the strongest known (p,γ) resonances, and a detector solid angle of nearly 2π sr was employed, we could only obtain a limit of $\Delta E = 0.3 \pm 0.6$ eV after two days of counting.

We then turned to the narrow ($\Gamma \sim 800$ eV) *s*-wave resonance in ^{27}Al(p,p) at $E_p = 1.35$ MeV, where $A_T = 0$ and thus uncertainties from transverse polarization effects are absent. The high efficiency of our proton detectors gave us a more sensitive means for measuring energy modulation than the (p,γ) technique. As the optimum target thickness for this measurement was ~ 7 μg/cm^2, the aluminum was evaporated onto the thinnest practical carbon foils (2–3 μg/cm^2), giving a sensitivity of $S_E^{\text{Al}} \approx 9 \times 10^{-5}$ eV^{-1} (see Fig. 25). We made three measurements of ΔE using the ^{27}Al resonance, two of which involved $\sim$ 1.5 days of counting with 200 nA of beam and achieved statistical accuracies of $\pm$0.2 eV.

Table VI summarizes the energy modulation measurements. The weighted average, $\Delta E = -0.18 \pm 0.14$ eV, shows little evidence for any energy modulation. However, as the A_L measurements were made under a wide variety of experimental conditions, and the source of any energy modulation was unknown, we adopted a more conservative upper limit of $|\Delta E| < 0.45$ eV by taking the weighted RMS value of the individual measurements plus a 1σ uncertainty. At E_{magic}, $S_E \leq 2 \times 10^{-6}$, so we could set the limit $A_z^{\Delta E} < 1 \times 10^{-6}$.

TABLE V. $\mathcal{A}_z(B/F)$ sensitivity to target thickness nonuniformities at E_{magic}.

Target No.	S_{tgt}^y (mm^{-1})	S_{tgt}^x (mm^{-1})	$\mathcal{A}_z^{\text{worst case}}(B/F)$
November 1986			
1	$-3.3 \pm 0.7 \times 10^{-3}$	$-3.4 \pm 0.2 \times 10^{-3}$	$< 1.3 \times 10^{-6}$
February 1987			
2	$3.4 \pm 0.8 \times 10^{-4}$	$-5.9 \pm 0.3 \times 10^{-4}$	$< 2.2 \times 10^{-7}$
3	$-9.9 \pm 0.2 \times 10^{-4}$	$-1.1 \pm 0.2 \times 10^{-4}$	$< 4.0 \times 10^{-7}$
September 1987			
4	$-3.9 \pm 1.1 \times 10^{-4}$	$1.6 \pm 0.3 \times 10^{-3}$	$< 6.8 \times 10^{-7}$
5	$-4.8 \pm 0.3 \times 10^{-4}$	$2.0 \pm 0.3 \times 10^{-4}$	$< 1.8 \times 10^{-7}$
6	$-0.8 \pm 0.3 \times 10^{-4}$	$-3.6 \pm 0.3 \times 10^{-4}$	$< 1.4 \times 10^{-7}$

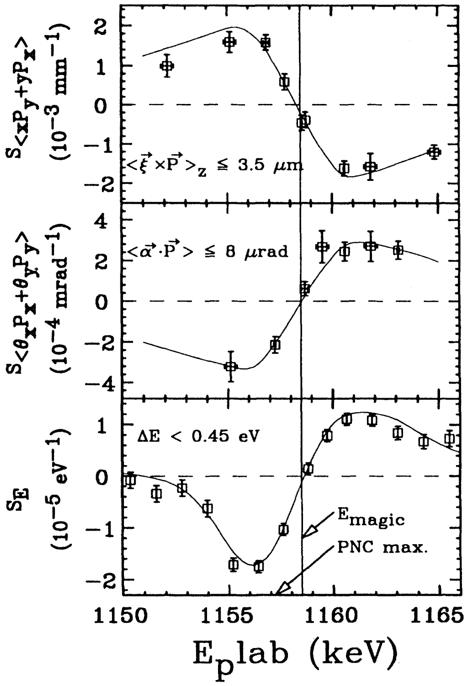

FIG. 25. Sensitivities to the three most important systematic effects as functions of the beam energy. All three sensitivities pass through zero within a 100 eV interval centered about 1.2 keV above the maximum of the PNC effect.

D. Spin-dependent effects

When the beam helicity was reversed, we observed that transverse components of the polarization changed sign as well. As the 0^+ resonance had a transverse analyzing power, this change in the transverse polarization components changed the distribution of the scattered intensity, which could have produced a false asymmetry. This could occur either by a net misalignment of the polarization or by a variation of the transverse polarization within the phase space of the beam [48].

1. Spin misalignment

Because of the symmetry of the detectors, a net spin misalignment (say $\langle P_y \rangle \neq 0$) only caused difficulty if there was a corresponding misalignment of the beam axis (say $\langle x \rangle \neq 0$). These false asymmetries were negligible as the transverse polarization components were nulled by the spin stabilizing loop, and the beam was kept along the symmetry axis by the beam stabilizing loops.

We determined the sensitivity to spin misalignment by measuring $\mathcal{A}_z$ with a transversely polarized beam deliberately displaced from the symmetry axis. At E_{magic}, the measured sensitivity was $S_{\langle x \rangle \langle P_y \rangle} < 2 \times 10^{-3}$ mm^{-1} and typical polarization misalignments were $P_\perp < 1.2 \times 10^{-3}$, establishing an upper limit of $\mathcal{A}_z^{\langle x \rangle \langle P_y \rangle}(B/F) < 2 \times 10^{-7}$. We obtained comparable limits on the false asymmetry caused by net spin misalignments (say $\langle P_x \rangle \neq 0$) coupled to a net angular misalignment of the beam (say $\langle \Theta_x \rangle \neq 0$).

2. Spin-position correlations

Transverse polarization variation can generate false effects if it is correlated with the finite phase space of the beam such that $\langle x P_y \rangle \neq 0$ or $\langle \Theta_x P_x \rangle \neq 0$. Such variations of residual transverse polarization within the beam presented a problem, as they could not be nulled with feedback loops.

We determined the sensitivities to transverse spin components, $S_{\langle x P_y \rangle}$ and $S_{\langle \Theta_x P_x \rangle}$, by measuring with a transversely polarized beam, the position and angle dependence of the longitudinal asymmetries at a series of energies across the 0^+ resonance. The sensitivities were extracted from the difference between measured asymmetries at two different beam positions(angles). The results are shown in panels 1 and 2 of Fig. 21. The solid lines are the computer model predictions.

Figure 22 shows an unusally large transverse polarization gradient measured with a strip-target scan of a beam whose net transverse polarization had been nulled. At the beam edges, the transverse polarization was nearly 2% or $\langle x P_y \rangle \approx 3.5$ μm. When multiplied by the measured sensitivity at E_{magic}, $S_{\langle x P_y \rangle} \leq 2.2 \times 10^{-4}$ mm^{-1}, this corresponded to a acceptably small asymmetry of $\mathcal{A}_z^{\langle x P_y \rangle}(B/F) = 8 \times 10^{-7}$.

3. Spin-angle correlations

We determined the spin-angle correlation by measuring the slope of the transverse asymmetries that resulted when we occluded portions of the beam as described in Sec. V B 2. Fortunately, at the energy of the maximum of the PNC effect we were less sensitive to spin-angle corre-

TABLE VI. Energy-modulation measurements.

Reaction	Measured asymmetry	S_E (eV^{-1})	Energy modulation (eV)
^{13}C(p,γ)	$21 \pm 42 \times 10^{-5}$	7×10^{-4}	0.30 ± 0.60
^{27}Al(p,p)	$-27 \pm 24 \times 10^{-6}$	6.9×10^{-5}	-0.39 ± 0.35
	$-38 \pm 17 \times 10^{-6}$	7.8×10^{-5}	-0.49 ± 0.22
	$6 \pm 16 \times 10^{-6}$	8.2×10^{-5}	0.07 ± 0.20
			$\lvert \Delta E \rvert < 0.45$ eV

lations than to spin-position correlations. A typical measured correlation of $\langle\theta_x P_x\rangle \leq 8$ μrad and the measured $S_{\langle\Theta_x P_x+\Theta_y P_y\rangle}$ shown in panel 2 of Fig. 21 corresponded to an acceptably small false effect of $\mathcal{A}_z^{\langle\theta_x P_x\rangle}(B/F) \leq 1.6 \times 10^{-7}$.

E. Electronic effects

A false asymmetry could have occurred if the signals from the two spin states were routed through separate electronic channels, or if ground loops coupled the state-changing electronics to the signal-processing electronics.

We symmetrized the detector electronics by transmitting from each detector a single logic signal that had a dead time greater than any subsequent elements in the counting chain. This signal was then fanned out by low dead-time discriminators into adjacent scaler banks. Furthermore, a routing switcher interchanged the functions of the scalers, so that for each pair of *reads* the spin states were averaged over the two scaler banks. Thus, the signal processing for the two routes was essentially identical. Test measurements using an α source set limits of $\mathcal{A}_z(B) < 1.8\times10^{-6}$. The routing asymmetry is probably substantially smaller, but it was too time consuming to reduce this limit further.

While the detector pulses were not sensitive to ground loops as digital signals were transmitted from the beamline to the data acquisition rack, the slit and cup currents were transmitted as analog signals and could be affected by ground loops. We minimized such effects by isolating the detectors and current-sensing devices from the beamline and grounded them only through the data acquisition rack. The logic signals that were correlated with spin state (signals that drove the RF transition units and that inhibited the scalers) were optically isolated to avoid ground loops. We tested for ground loop effects by running a loop, carrying an ≈ 1 A peak-to-peak current alternated at the spin-flip frequency, around the entire beamline and data acquisition rack. With a current source fed into the Faraday cup we measured $\mathcal{A}_z(I) < 2 \times 10^{-6}$ which was negligible compared to typical beam current asymmetries.

We concluded that electronic effects did not produce significant false asymmetries.

F. Summary of systematic effects

Our "worst case" upper limits on various contributions to the systematic error in $\mathcal{A}_z(B/F)$ are summarized in Table VII. The actual limits on these systematic errors for data taken with any given target are generally better than the values listed in the table. The overall systematic uncertainties given in Table III reflect the actual measured modulations and displacements for each target. The systematic error at an energy E_p was found by multiplying the "worst case" value for each systematic effect by the greatest sensitivity to that effect occurring anywhere in the energy interval from $E_p - \Delta E_p$ to $E_p + \Delta E_p$, where ΔE_p is the 1σ uncertainty in E_p. For example, at or near E_{magic} limits on energy-dependent effects (i.e., energy modulation and transverse polarization effects) were based on the calculated sensitivity at $E = E_{\text{magic}} \pm 120$ eV; the 120 eV error is a quadrature sum of the uncertainty in the energy of the measurement (about ±80 eV) and an uncertainty in the energy where the sensitivity crosses through zero (about ±90 eV).

The dominant systematic errors resulted from energy modulation, residual transverse polarization distributions, and target nonuniformity. The overall systematic uncertainty was found by adding these contributions in quadrature, except for the residual polarization effects in position and angle which were presumed correlated and were therefore added linearly. Limits on false asymmetries from most systematic effects were orders of magnitude smaller than the statistical accuracy of the A_L measurement, and errors from the dominant effects were still small compared to the expected PNC signal. We

TABLE VII. "Worst case" systematic error budget at E_{magic}.

Quantity	Measured modulation	Sensitivity	$\mathcal{A}_z^{\text{false}}(B/F)$
	Phase-space effects		
ΔI	$\leq 4 \times 10^{-2}$ nA	$\leq 1.5 \times 10^{-5}$ nA^{-1}	$\leq 6 \times 10^{-7}$
Δx (thickness)	$\leq 3.6 \times 10^{-4}$ mm	$\leq 3.6 \times 10^{-3}$ mm^{-1}	$\leq 1.3 \times 10^{-6}$
Δx (geometric)	"	$\leq 1.4 \times 10^{-4}$ mm^{-1}	$\leq 5 \times 10^{-8}$
$\Delta\sigma_x$	$\ll 8 \times 10^{-4}$ mm	$\approx 5 \times 10^{-5}$ mm^{-1}	$\ll 5 \times 10^{-8}$
$\Delta\theta$	$\leq 5 \times 10^{-4}$ mrad	$\leq 5 \times 10^{-5}$ mrad^{-1}	$\leq 3 \times 10^{-8}$
$\Delta\sigma_\theta$	$\leq 3 \times 10^{-4}$ mrad	$\approx 4 \times 10^{-5}$ mrad^{-1}	$\leq 1.2 \times 10^{-7}$
ΔE	< 0.45 eV	2.7×10^{-6} eV^{-1}	$< 1.2 \times 10^{-6}$
$\Delta\sigma_E$	-?-	1×10^{-4} eV^{-1}	-?-
	Transverse polarization effects		
$\langle x\rangle\langle P_y\rangle - \langle y\rangle\langle P_x\rangle$	$\leq 1.2 \times 10^{-4}$ mm	$\leq 2.2 \times 10^{-4}$ mm^{-1}	$\leq 2.6 \times 10^{-8}$
$\langle\theta_x\rangle\langle P_x\rangle + \langle\theta_y\rangle\langle P_y\rangle$	$\leq 7.2 \times 10^{-4}$ mrad	$\leq 2.4 \times 10^{-5}$ mrad^{-1}	$\leq 1.7 \times 10^{-8}$
$\langle xP_y - yP_x\rangle$	$\leq 3.5 \times 10^{-3}$ mm	$\leq 2.2 \times 10^{-4}$ mm^{-1}	$\leq 8 \times 10^{-7}$
$\langle\theta_x P_x + \theta_y P_y\rangle$	$\leq 8 \times 10^{-3}$ mrad	$\leq 2.4 \times 10^{-5}$ mrad^{-1}	$\leq 2 \times 10^{-7}$
	Electronic effects		
Routing asymmetry	–	–	Negligible
Ground loops	–	–	Negligible

concluded that at $E_{\rm magic}$ systematic effects contributed to A_L at a level below $\mathcal{A}_z^{\rm false}(B/F) = 1.5 \times 10^{-6}$, and that systematic corrections were not necessary.

VI. INTERPRETATION OF THE PNC EFFECT

A. General observations

The $\sim 5\sigma$ discrepancy between our result $\langle H_{\rm weak}\rangle = 0.38 \pm 0.26 \pm 0.09$ eV and two concordant shell-model predictions [23] based on the DDH "best value" PNC N-N interaction, $\langle H_{\rm weak}\rangle = -1.39$ eV and $\langle H_{\rm weak}\rangle = -1.04$ eV, was quite unexpected, as it was generally believed (see, for example, Ref. [1]) that shell-model calculations in a nucleus as simple as ^{14}N should be quite reliable. If, in fact, the shell-model matrix elements are correct, there would be a serious problem with the one-boson-exchange model of the PNC N-N interaction, as our result cannot be easily reconciled with other results for PNC matrix elements in ^{19}F, $\vec{p}+\alpha$, and ^{18}F as shown in Fig. 26. We therefore hesitate to draw such conclusions, and prefer to examine carefully the approximations in the nuclear structure calculations that might cause the predicted A_L in ^{13}C$(\vec{p},p)$ to be unreliable.

Several issues spring immediately to mind. The ^{14}N system differs in some significant ways from the other known parity doublets.

(1) The ^{14}N doublet is unbound, whereas the other parity doublets involve bound levels. The radial wave functions of unbound levels are not as well described by the conventional shell-model harmonic-oscillator functions as are those of well-bound levels.

(2) The configuration of the 0^+ level in ^{14}N is predominantly $2\hbar\omega$ in contrast with previously studied doublets where the natural-parity level was predominantly $0\hbar\omega$.

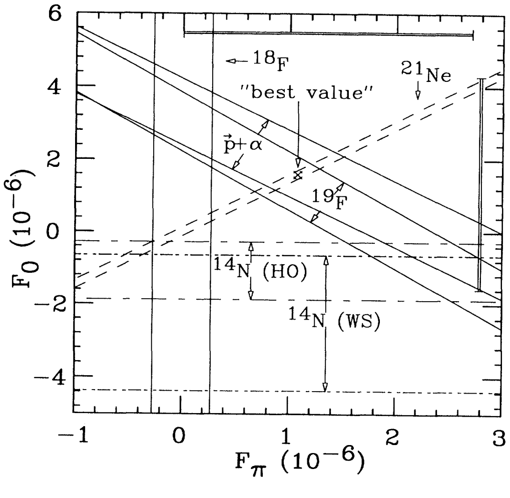

FIG. 26. Analysis of PNC effects in terms of the two dominant PNC MNN coupling constants F_π and F_0. The ^{14}N point is based on Haxton-Dubach calculation that is now known to be inadequate, while the ^{18}F and ^{19}F calculations are believed to be realistic. This plot illustrates the inconsistency that would arise if the ^{14}N calculation were assumed to be correct.

We have examined these and other theoretical issues with the help of W.C. Haxton and C. Johnson. Recently Horoi *et al.* [49], stimulated by our results, have presented a more elaborate analysis of parity mixing in the ^{14}N doublet. In this paper, therefore, we merely outline some of the issues.

1. *Effects of unbound single-particle wave functions*

The two-body matrix elements of PNC operators are usually evaluated using harmonic-oscillator (HO) wave functions (see, for example, Ref. [18]). However, in light nuclei the single-particle orbitals are often unbound and the infinite HO well does not generate realistic radial wave functions. The nuclear surface can be "softened" by including 1p-1h $2\hbar\omega$ excitations in the HO basis [18]. As the dominant component of the ^{14}N$(0_2^+;1)$ wave function is a 2p-2h $2\hbar\omega$ excitation, a 1p-1h $2\hbar\omega$ excitation beyond that requires a full $4\hbar\omega$ model space which imposes severe computational difficulties. Millener and Warburton [50] argued that it is preferable to evaluate the PNC matrix elements in a more realistic Woods-Saxon (WS) basis. However, one must then exclude $2\hbar\omega$ single-particle excitations that are implicitly included in the WS single-particle basis. In our case, this can be achieved by restricting the valence particles to the $1p$ and $2s1d$ shells. However, one cannot completely remove center-of-mass motion in this restricted basis.

The weak matrix element is dominated by the $2s_{1/2} \leftrightarrow 1p_{1/2}$ transition of the one-body PNC operator, $H_{\rm PNC} = K_0\vec{\sigma}\cdot\vec{p} + K_1\vec{\sigma}\cdot\vec{p}\tau_3$. Figure 27 compares the A dependence of this matrix element computed with HO and WS single-particle wave functions. The HO wave functions were calculated using the standard oscillator parameter $\hbar\omega = 41$ MeV$/A^{1/3}$. The WS wave functions were calculated using an optical potential fitted to the single-particle (hole) states of A=17 (15) with the well radii scaled as $A^{1/3}$. Isoscalar wave functions were produced by calculating wave functions using a unit nucleon charge and a well charge of $A/4$. The results in Fig. 27 indicate that for $A < 24$ the PNC matrix element becomes sensitive to the unbound character of the levels; by $A = 14$,

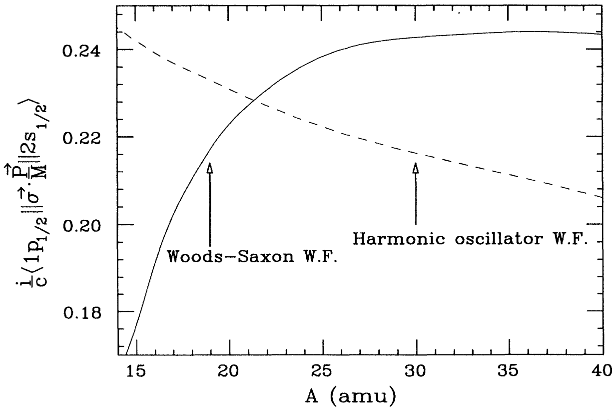

FIG. 27. Comparison of the one-body $2s_{1/2}$ to $1p_{1/2}$ PNC matrix elements computed using harmonic oscillator (HO) and Woods-Saxon (WS) wave functions for mass numbers between 15 and 21.

the one-body WS matrix element is reduced to roughly two-thirds of the standard HO value. We therefore modified Haxton's code, for calculating two-body PNC matrix elements to accept an arbitrary choice of single-particle basis states. Our calculations in ^{14}N agree qualitatively with the simple estimate above, indicating that the PNC matrix element is reduced substantially ($\sim$ 50%) when more realistic WS wave functions are employed. Horoi *et al.* [49] have recently found comparable effects in their calculations.

2. Effect of the dominant $2\hbar\omega$ configuration of the 0^+ state

In a typical parity doublet, such as that in ^{18}F, the 0^+ and 0^- wave functions are predominantly $0\hbar\omega$ and $1\hbar\omega$ respectively, with small admixtures of $2\hbar\omega$ and $3\hbar\omega$ configurations respectively. As shown in Fig. 28, the PNC operator cannot directly couple the $3\hbar\omega$ components of the 0^- level to the dominant $0\hbar\omega$ component of the 0^+ state, so that, to lowest order, the small components are included by considering only the $2\hbar\omega$ components in the 0^+ level. Because of charge-conjugation symmetry of the PNC operator, these $2\hbar\omega \leftrightarrow 1\hbar\omega$ contributions to $\langle H_{\text{weak}}\rangle$ interfere destructively with the dominant $0\hbar\omega \leftrightarrow 1\hbar\omega$ contributions [18]. In ^{14}N the situation is quite different because the 0^+ level is predominantly $2\hbar\omega$. As shown in Fig. 28, there are now *two* classes of first-order corrections to the dominant $2\hbar\omega \leftrightarrow 1\hbar\omega$ transitions: $0\hbar\omega \leftrightarrow 1\hbar\omega$ and $2\hbar\omega \leftrightarrow 3\hbar\omega$.

Horoi *et al.* [49] have investigated the effect of the $3\hbar\omega$ components of the $0_1^-;1$ state, and find that $3\hbar\omega$ configurations comprise 15% of the intensity of the 0^- wave function. Horoi *et al.* find that the $2\hbar\omega \leftrightarrow 3\hbar\omega$ amplitudes add coherently to the $2\hbar\omega \leftrightarrow 1\hbar\omega$ amplitudes, but they point out that these $2\hbar\omega \leftrightarrow 3\hbar\omega$ matrix elements should be viewed with caution, as they are very sensitive to the choice of single-particle energies.

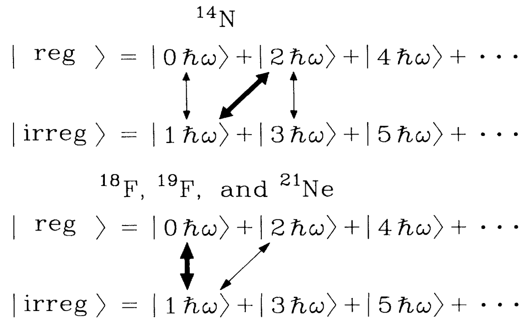

FIG. 28. Comparison of the weak matrix elements in ^{14}N and in other parity-mixed doublets. In the other parity doublets, the weak matrix element is dominated by the $0\hbar\omega$–$1\hbar\omega$ amplitude, with corrections arising from small admixtures of $2\hbar\omega$ excitations in the positive-parity state. In ^{14}N, the $0_2^+;1$ wave function is predominantly $2\hbar\omega$ so the dominant $0\hbar\omega$–$1\hbar\omega$ amplitude receives corrections from both $0\hbar\omega$ components of the positive-parity state and $3\hbar\omega$ components of the negative-parity state.

B. Comparison of theory and experiment

Table VIII compares the measured electromagnetic transition strengths, spectroscopic factors and the PNC

TABLE VIII. Comparison of theoretical estimates and measured properties of the $(0^+;1)_2$ and $(0^-;1)_1$ levels in ^{14}N.

		Shell-model estimates						
Observable	Experiment[a]	ZBM[b]	KB[c]	MK[d]	WB1[e]	WB2[f]	WB3[g]	WB4[h]
$B(M1)$ (μ_N^2)								
$(0^+;1)_2 \to (1^+;0)_1$	0.050 ± 0.005	0.32	$3.8 \cdot 10^{-5}$	0.075	0.031	0.012	0.084	0.014
$(0^+;1)_2 \to (1^+;0)_2$	1.05 ± 0.1		0.50	1.06	0.572	0.012	0.390	0.014
$(0^+;1)_2 \to (1^+;0)_3$	12.2 ± 1.2	12.7	12.1	12.0	11.31			
$B(E1)$ (e^2fm^2)								
$(0^+;1)_2 \to (1^-;0)_1$	0.0161 ± 0.0019	0.16	0.021	0.061	0.0042	0.0040	0.0029	0.0015
$(0^-;1)_1 \to (1^+;0)_1$	0.0355 ± 0.0028	0.086		0.027	0.015			
C^2S ($^{14}\text{N}^* \to {}^{13}\text{C}_{\text{g.s.}} + p$)								
$(0^+;1)_2$	0.022	0.045	0.091	0.065			0.026	0.068
$(0^-;1)_2$	0.38	0.50	0.39	0.39			0.477	0.477
H_{weak} (eV)	0.38 ± 0.28	−1.39	−0.29	−0.56	−0.49	−0.23	−0.76	−0.50

[a] This work.
[b] ZBM model from reference [23].
[c] $(0+1+2)\hbar\omega$ with bare Kuo $2\hbar\omega$ interaction [51].
[d] $(0+1+2)\hbar\omega$ with Millener-Kurath $2\hbar\omega$ interaction [51].
[e] $(0+1+2+3)\hbar\omega$ with Warburton-Brown WBT interaction [49].
[f] Same as WB1 but including $4\hbar\omega$ excitations for the natural parity states.
[g] $(0+1+2+3)\hbar\omega$ with Warburton-Brown WBT interaction with a modified *p-sd* gap [49].
[h] Same as WB3 but including $4\hbar\omega$ excitations for the natural parity states.

matrix element in ^{14}N to seven recent shell-model estimates. The wave functions from the original Haxton-Dubach calculation were unfortunately not available for this comparison. Only four of the large model-space calculations by Horoi *et al.* are shown as a complete account of their work is already available [49].

The Haxton and Johnson $(0+1+2)\hbar\omega$ calculation [51] using the Millener-Kurath interaction best reproduces the electromagnetic transition rates, but overpredicts by a factor of 3 the $(0^+;1)_2$ spectroscopic factor. Horoi *et al.*'s predictions for the $0^+;1$ spectroscopic factor are in much better agreement with experiment, but Horoi *et al.* tend to underpredict the $E1$ strengths, while their $M1$ strengths vary widely due to sensitive cancellations between different components of the wave functions. Thus none of the models reproduces all of the important parity-conserving observables in the ^{14}N doublet. Furthermore, reasonable variations in the model parameters, such as the single-particle energies, produce markedly different results.

The last row in Table VIII gives the theoretical estimates for the PNC matrix element; all calculations use the "best value" PNC N-N amplitudes of Desplanques, Donoghue, and Holstein [2]. In every case, the *sign* of the predicted matrix elements is opposite to the measured value. However, in the larger model spaces, the *magnitude* of the predicted weak matrix element is reduced enough to be consistent with the experimental magnitude. A decomposition of the matrix elements indicates that cancellations are predominantly responsible for the variations seen among the different calculations. If the magnitudes of the individual two-body matrix elements are summed, the total available PNC strength is about 1.5 eV. Thus, matrix elements of around 0.3 eV indicate cancellation by a factor of 5. The extensive cancellation in the more sophisticated models (as compared to nearly no cancellation in the ZBM model) indicates that careful attention to the small components of the wave functions and accurate reproduction of parity-conserving properties is a necessary first test for believable calculations of the weak matrix element. In light of these theoretical uncertainties, we conclude that it would be premature to draw conclusions about the MMN PNC coupling constants from our experimental result.

VII. CONCLUSIONS

The discrepancy between our PNC result and the existing shell-model calculations has led us to reanalyze assumptions made in essentially all shell-model calculations of PNC nuclear matrix elements. We find the nuclear structure of the ^{14}N doublet to be qualitatively different from that of the ^{18,19}F and ^{21}Ne doublets. One must therefore pay careful attention to aspects (such as the exact form of the radial wave functions, the $3\hbar\omega$ components of the negative parity state, and the $4\hbar\omega$ components of the positive parity level) that occur to a lesser degree in all parity doublets. Now that full $4\hbar\omega$ shell-model calculations are becoming feasible, these nuclear structure questions can be fully addressed. A first attempt has recently been reported [49] with results for $\langle H_{\mathrm{weak}}\rangle$ that are in significantly better agreement with experiment. However, even these calculations do not reproduce important parity-conserving observables (such as $E1$ transition rates). Furthermore, the calculated weak matrix element remains quite sensitive to the model assumptions. Once these issues have been resolved our work should not only provide a reliable constraint on the isoscalar weak ρ-exchange coupling constant, but it will have established the framework for improved analyses of other parity doublets as well.

ACKNOWLEDGMENTS

Two persons whose names are not on the author list made significant contributions to this work. M.Z. Iqbal designed our complicated scattering chamber (writing a three-dimensional visualization program to do so), and J.L. Osborne, before his untimely death, wrote the original analysis program and helped in the early efforts to debug the apparatus. We appreciated their contributions and regret that neither of them could participate in the data-taking phase of this experiment. We are grateful to W.C. Haxton and C. Johnson for many informative conversations about the implications of our result, and to M. Horoi for extending his ^{14}N calculations expressly for our comparison. V.Z. thanks his collaborators at Carnegie Mellon University for allowing him to complete this paper while working on new projects with their group. The researchers at Seattle and Madison were supported in part by the Department of Energy and the National Science Foundation respectively.

---

[1] E.G. Adelberger and W.C. Haxton, Annu. Rev. Nucl. Part. Sci. **35**, 501 (1985).

[2] B. Desplanques, J.F. Donoghue, and B.R. Holstein, Ann. Phys. **124**, 449 (1980).

[3] J.M. Potter, J.D. Bowman, C.F. Hwang, J.L. McKibben, R.E. Mischke, P.B. Debrunner, H. Frauenfelder, and L.J. Sorenson, Phys. Rev. Lett. **33**, 1307 (1974).

[4] D.E. Nagle, J.D. Bowman, C.F. Hwang, J.L. McKibben, and R.E. Mischke, in *Proceedings from the 3rd International Conference on High Energy Beams and Polarized Targets*, Argonne, 1978, edited by G.H. Thomas, AIP Conf. Proc. No. 51 (AIP, New York, 1979).

[5] R. Balzer, R. Henneck, Ch. Jacquemart, J. Lang, F. Nessi-Tedaldi, T. Roser, M. Simonius, W. Haeberli, S. Jaccard, W. Reichart, and Ch. Weddigen, Phys. Rev. C **30**, 1409 (1984).

[6] S. Kistryn, J. Lang, J. Liechti, Th. Maier, R. Müller, F. Nessi-Tedaldi, M. Simonius, J. Smyrski, S. Jaccard, W. Haeberli, and J. Sromicki, Phys. Rev. Lett. **58**, 1616 (1987).

[7] V.A. Knyazkov, E.A. Kolomenskii, V.M. Lobashov, V.A. Nazarenko, A.N. Pirozhov, A.I. Shabii, E.V. Shul'gina, Y.V. Sobolev, and A.I. Yegorov, Nucl. Phys. **A417**, 209 (1984).

[8] J.F. Caviagnac, B. Vignon, and R. Wilson, Phys. Lett. B **54**, 148 (1977).

[9] C.A. Barnes, M.M. Lowry, J.M. Davidson, R.E. Marrs, F.B. Morinigo, B. Chang, E.G. Adelberger, and H.E. Swanson, Phys. Rev. Lett. **40**, 840 (1978).

[10] G. Ahrens, W. Harfst, J.R. Kasš, E.V. Mason, and M.

Schober, Nucl. Phys. **A390**, 486 (1982).

[11] H.C. Evans, G.T. Ewan, S.-P. Kwan, J.R. Leslie, J.D. MacArthur, H.-B. Mak, W. McLatchie, S.A. Page, P. Skensved, S.-S. Wang, A.B. McDonald, C.A. Barnes, T.K. Alexander, and E.T.H. Clifford, Phys. Rev. Lett. **55**, 791 (1985).

[12] M. Bini, T.F. Fazzini, G. Poggi, and N. Taccetti, Phys. Rev. Lett. **55**, 795 (1985).

[13] E.G. Adelberger, H.E. Swanson, M.D. Cooper, W. Tape, and T.A. Trainor, Phys. Rev. Lett. **41**, 1975 (402); E.G. Adelberger, in *Polarization Phenomena in Nuclear Physics—1980*, Santa Fe, New Mexico, edited by G.G. Ohlsen, R.E. Brown, N. Jarmie, W.W. McNaughton, and G.M. Hale, AIP Conf. Proc. No. 69 (AIP, New York, 1981), p. 1367.

[14] K. Elsener, W. Grüebler, V. König, P.A. Schmelzbach, J. Ulbricht, B. Vuaridel, D. Singy, C. Forstner, and W.Z. Zhang, Nucl. Phys. **A461**, 579 (1987).

[15] K.A. Snover, R. Von Lintig, E.G. Adelberger, H.E. Swanson, T.A. Trainor, A.B. McDonald, E.D. Earle, and C.A. Barnes, Phys. Rev. Lett. **41**, 145 (1978).

[16] J. Lang, Th. Maier, R. Müller, F. Nessi-Tedaldi, Th. Roser, M. Simonius, J. Sromicki, and W. Haeberli, Phys. Rev. Lett. **54**, 170 (1985); Phys. Rev. C **34**, 1545 (1986).

[17] E.G. Adelberger, C.D. Hoyle, H.E. Swanson, and R.D. Von Lintig, Phys. Rev. Lett. **46**, 695 (1981).

[18] W.C. Haxton, Phys. Rev. Lett. **46**, 698 (1981).

[19] E.G. Adelberger, M.M. Hindi, C.D. Hoyle, H.E. Swanson, R.D. Von Lintig, and W.C. Haxton, Phys. Rev. C **27**, 2833 (1983).

[20] K. Neubeck, H. Schober, and H. Wäffler, Phys. Rev. C **10**, 320 (1974).

[21] An experiment designed to measure neutron spin rotation through a para-hydrogen target is presently under development at Seattle. The sensitivity is expected to be good enough to provide significant constraints on the PNC *n-p* interaction.

[22] V.J. Zeps, Ph.D. thesis, University of Washington (1989).

[23] E.G. Adelberger, P. Hoodboy, and B.A. Brown, Phys. Rev. C **30**, 456 (1984); **33**, 1840 (1986).

[24] F. Ajzenberg-Selove, Nucl. Phys. **A523**, 1 (1991).

[25] R.J. Peterson and J.J. Hamill, Nucl. Phys. **A362**, 163 (1981).

[26] R.J. Peterson, H.C. Bhang, J.J. Hamill, and T.J. Masterson, Nucl. Phys. **A425**, 469 (1984).

[27] Calculation using unpublished wave functions of J. Dubach and W.C. Haxton reported in Ref. [23].

[28] C. Bloch, Nucl. Phys. **A4**, 503 (1957).

[29] P.G. Bizzeti, Phys. Rev. C **33**, 1837 (1986).

[30] F. Ajzenberg-Selove, Nucl. Phys. **A449**, 1 (1986).

[31] P.B. Fernandez, E.G. Adelberger, K.A. Snover, C.A. Gossett, J.L. Osborne, and V.J. Zeps, Nuclear Physics Lab Annual Report, University of Washington, 1985, p. 65.

[32] P.M. Endt and C. Van der Leun, Nucl. Phys. **A310**, 1 (1978).

[33] E.G. Adelberger, R.E. Marrs, K.A. Snover, and J.E. Bussoletti, Phys. Rev. C **15**, 484 (1977).

[34] C. Rolfs, Nucl. Phys. **A217**, 29 (1973).

[35] F. Riess, W.J. O'Connell, and P. Paul, Nucl. Phys. **A175**, 462 (1971).

[36] C. Pruneau, M.B. Chatterjee, C. Rangacharyulu, and C. St-Pierre, Can. J. Phys. **63**, 1141 (1985).

[37] F.W. Prosser, Jr., R.W. Krone, and J.J. Singh, Phys. Rev. **129**, 1716 (1963).

[38] R.F. Christy and I. Duck, Nucl. Phys. **24**, 89 (1961).

[39] V.J. Zeps, unpublished.

[40] F.C. Barker, private communication.

[41] J.D. King, Can. J. Phys. **69**, 828 (1991).

[42] V.A. Latorre and J.C. Armstrong, Phys. Rev. **144**, 892 (1966).

[43] W. Haeberli, M.D. Barker, C.A. Gossett, D.G. Mavis, P.A. Quin, J. Sowinski, T. Wise, and H.F. Glavish, Nucl. Instrum. Methods **196**, 319 (1982).

[44] J.F. Janni, At. Data Nucl. Data Tables **27**, 1 (1982).

[45] C.A. Gossett, E.G. Adelberger, V.J. Zeps, and J. Sromicki, Bull. Am. Phys. Soc. **31**, 1209 (1986).

[46] S. Tharraketta, W. Arnold, H. Baumgart, J. Günzel, A. Hoffman, E. Huttel, N. Kniest, and G. Clausnitzer, in *Proceedings of the Sixth International Symposium on Polarization Phenom. in Nucl. Phys.*, Osaka, Japan [J. Phys. Soc. Jpn. **55**, 880 (1986)].

[47] J. Sromicki, P.A. Quin, W. Haeberli, E.G. Adelberger, C.A. Gossett, H.E. Swanson, and V.J. Zeps, Nucl. Instrum. Methods **A255**, 611 (1987).

[48] M. Simonius, R. Henneck, Ch. Jacquemart, J. Lang, W. Haeberli, and Ch. Weddigen, Nucl. Instrum. Methods **177**, 471 (1980).

[49] M. Horoi, G. Clausnitzer, B. A. Brown, and E. K. Warburton, Phys. Rev. C **50**, 775 (1994).

[50] D.J. Millener and E.K. Warburton, in *Proceedings of the International Symposium on Nuclear Shell Models*, Philadelphia, Pennsylvania, 1984, edited by M. Vallieres and B.H. Wildenthal (World Scientific, Singapore, 1984), p. 365.

[51] W.C. Haxton and C. Johnson, unpublished.